VOL. 53, NO. 20 JOURNAL OF THE ATMOSPHERIC SCIENCES 15 OCTOBER 1996

Structure and Evolution of the 22 February 1993 TOGA COARE Squall Line: Numerical Simulations

S. B. TRIER, W. C. SKAMAROCK, M. A. LEMONE, AND D. B. PARSONS

National Center for Atmospheric Research, Boulder, Colorado*

D. P. JORGENSEN

NOAA/NSSL/Mesoscale Research Division, Boulder, Colorado

(Manuscript received 22 August 1995, in final form 8 February 1996)

ABSTRACT

In this study a numerical cloud model is used to simulate the three-dimensional evolution of an oceanic tropical squall line observed during the Tropical Ocean Global Atmosphere Coupled Ocean–Atmosphere Response Experiment and investigate the impact of small-scale physical processes including surface fluxes and ice microphysics on its structure and evolution. The observed squall line was oriented perpendicular to a moderately strong low-level jet. Salient features that are replicated by the model include an upshear-tilted leading convective region with multiple updraft maxima during its linear stage and the development of a 30-km scale midlevel vortex and associated transition of the line to a pronounced bow-shaped structure.

In this modeling approach, only surface fluxes and stresses that differ from those of the undisturbed environment are included. This precludes an unrealistically large modification to the idealized quasi-steady base state and thus allows us to more easily isolate effects of internally generated surface fluxes and stresses on squall line evolution. Neither surface fluxes and stresses nor ice microphysics are necessary to simulate the salient features of the squall line. Their inclusion, however, results in differences in the timing of squall line evolution and greater realism of certain structural characteristics. Significant differences in the convectively induced cold pool strength occur between the early stages of simulations that included ice microphysics and a simulation that contained only warm-rain microphysical processes. The more realistic strength and depth of the cold pool in the simulations that contained ice processes is consistent with an updraft tilt that more closely resembles observations. The squall-line-induced surface fluxes also influence the strength but, more dramatically, the areal extent of the surface cold pool. For the majority of the 6-h simulation, this influence on the cold pool strength is felt only within several hundred meters of the surface. Significant impact of squall-line-induced surface fluxes on the evolving deep convection at the leading edge of the cold pool is restricted to the later stages ($t \geq 4$ h) of simulations and is most substantial in regions where the ground-relative winds are strong and the convectively induced cold pool is initially weak and shallow.

1. Introduction

The Tropical Ocean Global Atmosphere (TOGA) Coupled Ocean–Atmosphere Response Experiment (COARE) was conducted over the equatorial western Pacific Ocean from November 1992 to March 1993. This paper represents the first part of a study in which we report on fully three-dimensional simulations of a well-documented mesoscale convective system (MCS) that occurred during TOGA COARE. Our primary focus concerns the mesoscale organization of convection and the relationship between deep convection and the surface fluxes of the ocean–atmosphere interface, both of which are key scientific objectives of TOGA COARE (Webster and Lukas 1992).

The specific goals of the current paper are to examine general characteristics of a numerical simulation of the observed MCS and, through a series of supporting numerical simulations, to isolate the influences of small-scale physical processes including ice microphysics and surface fluxes on MCS structure and evolution. Not only do the effects of MCS downdraft-induced cold pools on surface fluxes need to be accounted for in large-scale models, but the feedbacks between these surface fluxes and deep convection may need to be accounted for as well. Global models have already exhibited a strong sensitivity to the treatment of fluxes in light-wind conditions (Miller et al. 1992) and in as-

---

* The National Center for Atmospheric Research is sponsored by the National Science Foundation.

Corresponding author address: Stanley B. Trier, National Center for Atmospheric Research, P.O. Box 3000, Boulder, CO 80307-3000. E-mail: trier@ncar.ucar.edu sociation with downdrafts (Arakawa and Cheng 1993). In this paper, we use an idealized approach to focus on a specific aspect of the feedback process between surface fluxes and deep convection that has not been widely studied, namely the influence of surface fluxes generated *internally* by MCSs on MCS structure and evolution.

The MCS studied here belongs to a broad class of precipitation systems that have been commonly observed in midlatitude (e.g., Newton 1950; Smull and Houze 1985, 1987; Johnson and Hamilton 1988; Rutledge et al. 1988; Carbone et al. 1990; Houze et al. 1989), tropical (e.g., Houze 1977; Zipser 1977; Chong et al. 1987; Keenan and Carbone 1992), and subtropical (e.g., Wang et al. 1990) environments, in which a significant amount of low-level vertical wind shear is directed perpendicular to the leading edge of active convection. The more intense examples of these systems are typically classified as squall lines and are characterized by rapid movement; gusty surface winds; abrupt changes of pressure, temperature, and humidity at the leading edge; and in some cases the development of an extensive region of trailing stratiform precipitation. Fast-moving squall-type precipitation systems form a subset of Rickenbach's (1995) large, linear "type 3" systems that he found to be responsible for 57% of the rainfall observed by shipboard Doppler radars during the 4-month COARE field phase.

Both surface fluxes and ice microphysical processes influence the properties of the subcloud cold pools associated with squall lines. Numerical simulations (e.g., Thorpe et al. 1982; Rotunno et al. 1988) have firmly established that once initiated, squall lines can be maintained through new updrafts generated by the interaction of the storm-induced cold pool and the component of the environmental vertical shear normal to its leading edge. A key objective of the current paper is to examine the extent to which the small-scale physical processes of surface fluxes and stresses and ice microphysics impact this fundamental squall line maintenance mechanism. For the tropical oceanic environment, where cold pools and the environmental vertical shear are weak in comparison to their midlatitude counterparts, one might expect that their interactions are more sensitive to surface fluxes and ice microphysics. Possible evidence for such sensitivities has come from previous two-dimensional numerical simulations that have documented differences in cold pool propagation speeds for different microphysical parameterizations for Global Atmospheric Research Program Atlantic Tropical Experiment convection (Ferrier et al. 1995) and differences in precipitation rates with the inclusion of surface fluxes in Taiwan Area Mesoscale Experiment convection (Tao et al. 1991).

Our numerical studies complement an analysis of aircraft observations to be reported in a companion study for which preliminary results are found in Jorgensen et al. (1995) and LeMone et al. (1995). The squall line was observed using in situ flight level and Doppler radar measurements from two NOAA P-3 aircraft over the southeastern portion of the TOGA COARE experiment area near the Solomon Islands on 22 February 1993. Satellite imagery indicated that the squall line was situated at the eastern leading edge of a much larger cloud cluster that extended westward nearly 1000 km. The ~3 h of data collection was concentrated within 120 km of the NNW–SSE oriented leading edge of the precipitation system. During this period the quasi-linear leading convective band of large radar reflectivity ($Z > 35$ dBZ) originally aligned approximately perpendicular to the low-level vertical wind shear, evolved to a three-dimensional bow-shaped structure, and then weakened as it approached Guadalcanal within the Solomon Island chain (Fig. 1). Jorgensen et al. (1995) showed that the transition from the linear to bow-shaped structure (Figs. 1a,b) was accompanied by development of a ~30-km-scale vortex near the northern end of the bowed segment. This portion of the convective band subsequently surged eastward ahead of the remainder of the leading edge (Fig. 1c).

The present case offers an opportunity to examine the dynamics of a well-documented squall line that evolves into a highly three-dimensional precipitation system. As noted earlier, the basic two-dimensional maintenance mechanism for this type of convective system has already been well established. However, the three-dimensional evolution of such systems is not fully understood and remains an active area of observational (Brandes 1990; Jorgensen and Smull 1993; Loehrer and Johnson 1995; Scott and Rutledge 1995) and numerical (Weisman 1993; Davis and Weisman 1994; Skamarock et al. 1994) research. Recent simulations in midlatitude environments of large convective available potential energy (CAPE) have illustrated the importance of tilting of horizontal vorticity associated with both environmental (Weisman 1993) and MCS-generated vertical shear (Davis and Weisman 1994), and the convergence of planetary vertical vorticity (Skamarock et al. 1994; Davis and Weisman 1994) in the development of mesoscale vortices and the related three-dimensional evolution of finite-length squall-type convective systems. There are similarities in the evolution of the observed tropical squall line to midlatitude systems despite its occurrence in a smaller-CAPE near-equatorial (weakly rotating) environment. In this paper we show that the numerical model is capable of simulating major features of its observed three-dimensional evolution, including the development of mesoscale vortices and bow-shaped leading edge, and structural characteristics of the convective-scale motions. A more detailed analysis of the dynamics of these features will be presented in the next paper in our series of numerical studies.

The current paper is organized as follows. In section 2 we discuss the numerical model and design of sim-

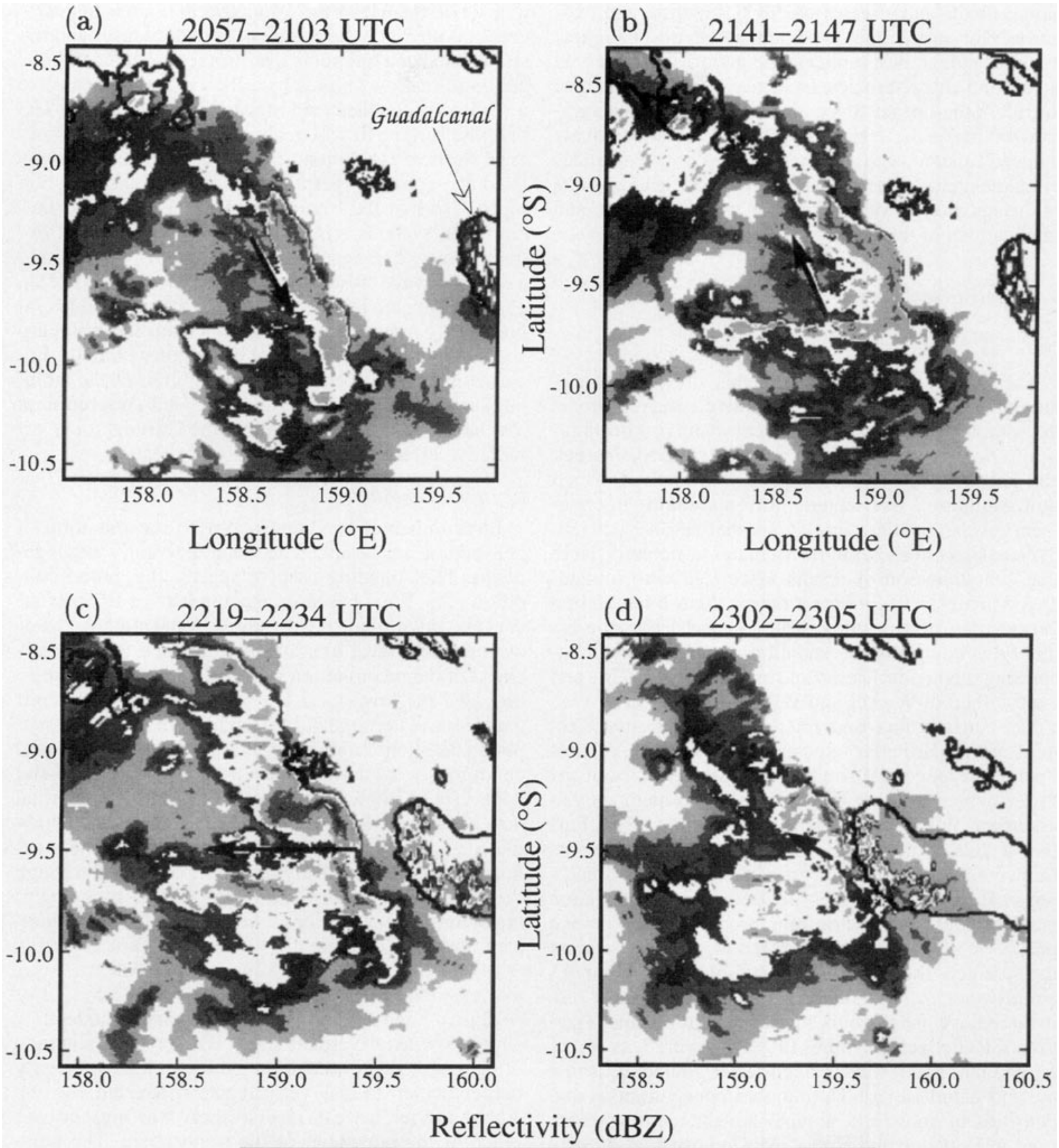

FIG. 1. P-3 lower-fuselage Doppler radar reflectivity scans taken from (a) 2057–2103, (b) 2141–2147, (c) 2219–2234, and (d) 2302–2305 UTC 22 Feb 1993. Plotting domain is 240 km × 240 km. Aircraft flight legs are indicated by the bold arrows. Boundaries of islands within the Solomon Archipelago are denoted by the bold solid lines.

ulations. The general evolution and vertical structure found in the series of simulations are presented in sections 3 and 4, respectively. These sections blend model sensitivity studies and comparisons with the more relevant aircraft observations in an effort to assess the impact of ice microphysics, and surface thermodynamic fluxes and stresses on MCS structure and evolution. Not surprisingly, we find that the most complete model is able to best replicate the majority of observed squall line characteristics. In section 5, we examine the impact of the surface flux and ice microphysical parameterizations on the vertical structure of the convectively induced subcloud cold pool and discuss how this relates to maintenance of deep convection at the leading edge of the squall-type MCS. We close with a summary and implications of this work in section 6.

2. Experimental design

a. Numerical model

The numerical model used in this study is a three-dimensional, nonhydrostatic primitive equation model that employs the fully automated adaptive-grid algorithms described in Skamarock (1989) and Skamarock and Klemp (1993). The adaptive-grid method, which utilizes multiple overlapping grids and multiple refinement levels, enables simulations that resolve convective-scale motions within a domain sufficiently large that contamination of results associated with limited-area domains is insignificant during the 6-h integration period used in this study. The solution technique for the fully compressible equations employs the time-splitting method of Klemp and Wilhelmson (1978) and is described in Wicker and Wilhelmson (1995).

The surface flux and microphysical parameterizations are of particular relevance to this study. Vertical fluxes and tangential stresses are parameterized at the lower boundary using bulk aerodynamic methods that assume a constant sea surface temperature (SST). Further details of the surface boundary condition and its implementation are given in section 2c. Two microphysical parameterizations are used. For the simulation that includes only warm-rain processes and no ice phase, we use the Kessler (1969) bulk parameterization that predicts the water categories of water vapor q_v, cloud water q_c, and rain q_r. When ice processes are included, we use the bulk microphysical parameterization of Rutledge and Hobbs (1984) that predicts q_v, q_c, q_r, and the frozen water categories of graupel q_g, snow q_s, and cloud ice q_i. The number concentrations and densities of snow and graupel are the same as those used in Rutledge and Hobbs. McCumber et al. (1991) discussed the strong sensitivity of surface precipitation distribution to these parameters and concluded that the values used by Rutledge and Hobbs result in realistic simulations of squall lines and convective bands in the tropical oceanic GATE environment. Subgrid-scale turbulent mixing is represented in the model using a first-order closure similar to that of Clark (1979).

In all simulations presented in this paper, a horizontal domain of 540 km × 540 km with horizontal grid resolutions of 9, 3, and 1 km are used. The model depth is 24.5 km. A vertical velocity threshold is employed to activate the use of the 1-km grid in regions of active convection. Since the presquall boundary layer and the storm-induced cold pools over tropical oceanic regions are quite shallow (typically ~1 km or less), we utilize a vertically stretched grid in which Δz varies from 100 m at the surface to 700 m above 8 km to enhance low-level vertical resolution. The model domain is translated at a constant speed of 10.6 m s^{-1} in the direction of 101° so that the leading edge of the simulated precipitation systems remain reasonably close to the domain center. The upper boundary is rigid ($w = 0$), and a gravity wave absorbing layer (Durran and Klemp 1983) is situated between 17 and 24.5 km. Open lateral boundary conditions, described in Klemp and Wilhelmson (1978), are used on the coarse outer domain. Because of the relatively short 6-h duration of the simulations and the location of the observed convection at low latitudes (9°–10°S), neither the Coriolis force nor radiative effects are included.

b. Initial conditions

Environmental conditions prior to the initiation of convection are assumed to be horizontally homogeneous. The sounding used to specify this initial condition (Fig. 2) is based on a composite of P-3 aircraft data and rawinsonde observations from Honiara, Guadalcanal. Low-level aircraft data obtained immediately ahead of the precipitation system during its linear stage provided the lowest 1.3 km of the sounding. Aircraft data from a later time during the bow-shaped stage supplied conditions from 1.3 to 6 km. Above 6 km, initial conditions were derived from a blend of the 1800 and 2400 UTC 22 February Honiara soundings. The initial data at each vertical grid point in the simulation is tabulated in the appendix. The CAPE for irreversible pseudoadiabatic ascent of an air parcel averaged through the lowest 50 mb is ~1500 J kg^{-1}. The sounding is moist throughout the troposphere. The minimum equivalent potential temperature θ_e (338–340 K), departing ~15 K from surface conditions, is present in a layer that extends from 2 to 4 km MSL. A low-level jet of ~12 m s^{-1} centered at 2 km MSL results in moderately strong low-level vertical shear. The mean orientation of the major axis of the observed squall line was nearly perpendicular to the vertical shear beneath the jet. Above the jet, a weak reverse shear was present over much of the remainder of the troposphere. The moderate CAPE and significant component of the low-level vertical shear oriented parallel to MCS leading-edge propagation are similar to what was found in environments of fast-moving squall lines observed over the tropical Atlantic Ocean during GATE (Barnes and Sieckman 1984).[1]

---

[1] CAPE was 500 J kg^{-1} less and the jet level was located 1.5–2 km higher for the Barnes and Sieckman composite of the GATE fast-moving squall line environment.

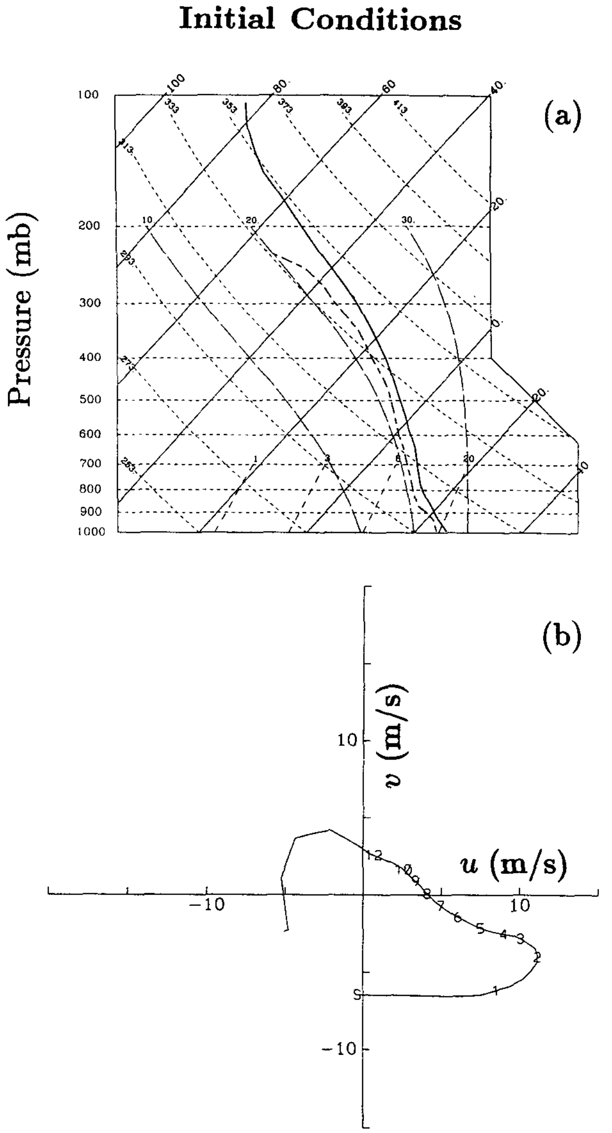

FIG. 2. (a) Temperature (solid) and dewpoint (dashed) curves in °C, and (b) hodograph (m s^{-1}) used to specify the initial condition in the numerical model. In (b), numbers indicate height in km above mean sea level. Numerical values at each model level are provided in the appendix.

c. Implementation of surface fluxes

The surface tangential stresses and vertical fluxes were calculated at each time step in the model using the bulk aerodynamic formulas

$$\tau_{xz} = (C_D u |\mathbf{v}_H|)_{\Delta z/2} \quad (1)$$

$$\tau_{yz} = (C_D v |\mathbf{v}_H|)_{\Delta z/2} \quad (2)$$

$$F_z^{\theta} = (C_H |\mathbf{v}_H|)_{\Delta z/2}(\theta_{\text{sfc}} - \theta|_{\Delta z/2}) \quad (3)$$

$$F_z^{q_v} = (C_E |\mathbf{v}_H|)_{\Delta z/2}(q_{\text{ssfc}} - q_v|_{\Delta z/2}), \quad (4)$$

where $\Delta z/2 = 50$ m, the lowest model grid point at which the horizontal wind components (u, v) are stored. In these expressions C_D, C_H, and C_E represent the drag coefficient, and exchange coefficients for heat and moisture, respectively. The variables θ_{sfc} and q_{ssfc} refer to the potential temperature associated with a constant SST of 27.8°C (chosen from a mean value estimated using downward-looking radiometer data from the P-3 aircraft) and its corresponding value of water vapor saturation mixing ratio, respectively. The idealization of constant SST, applied over 6 h, is justified by observations. The air–sea temperature difference for the ambient environment was 1.3°C. The aircraft measurements from legs flown within the disturbed region of the convective system suggest maximum SST changes from the preconvective environment of $-0.2°$ to $-0.5°$C. These changes are roughly an order of magnitude less in absolute value than the measured air–sea temperature differences within and immediately rearward of the active convection region, consistent with the composite of 42 MCS wakes during TOGA COARE presented by Young et al. (1995).

Following Rotunno and Emanuel (1987), the exchange coefficients for heat and moisture are set equal to the drag coefficient and are defined by

$$C_D = 1.1 \times 10^{-3} + 4 \times 10^{-5} |\mathbf{v}_H|_{z=50\,\text{m}}. \quad (5)$$

A more sophisticated surface flux formulation (Fairall et al. 1996) has been developed for the light wind environment typical of TOGA COARE. In the TOGA COARE flux routine, as well as in a similar earlier formulation (Liu et al. 1979), the drag and exchange coefficients depend on factors in addition to wind speed, including static stability, and are, in general, not equal. In these routines, the drag coefficient and exchange coefficients are obtained iteratively, which results in significantly greater amounts of computation if the fluxes are to be determined at each model time step. The lesser amount of computation, along with realistic results obtained in previous simulations within strong wind environments, influenced our choice of the simpler formulation (5). Surface wind speeds in the current case, which ranged from an undisturbed value of 7 m s^{-1} to disturbed values as large as 18 m s^{-1}, are less than those found in the tropical cyclone environment of Rotunno and Emanuel (1987) but significantly larger than average values observed during TOGA COARE (Lin and Johnson 1996). The ambient sensible and latent heat fluxes, computed using (3)–(5), are 10 W m^{-2} and 90 W m^{-2}, respectively.

The forces that determine the structure of the undisturbed (base state) tropical marine boundary layer, which has been observed to be relatively steady on the temporal and spatial scales of interest in our simulations (e.g., LeMone 1980), interact in a complex manner over a wide range of atmospheric scales. Among these forces and their associated processes, the necessary surface momentum sources (e.g., large-scale pressure gradients, large-scale advection) and heat and moisture sinks (e.g., radiative fluxes, nonprecipitating boundary layer cumulus clouds, large-scale advection) that help balance the effects of the surface fluxes and stresses in nature are not present in our idealized model framework. As a result, direct inclusion of the surface fluxes and stresses leads to an unrealistic evolution of the model base state. Application of (1)–(5) to the environmental sounding in the model reveals that forcing solely from the ambient surface fluxes and stresses results in average 6-h increases through the lowest 500 m in θ and q_v of 0.4°C and 1.0 g kg^{-1}, respectively. The average wind speed in the lowest 500 m decreases 1.4 m s^{-1} during this period. These modifications to the lower levels result in an increase in CAPE from ~1500 to 2300 J kg^{-1} and potentially significant changes in low-level vertical shear. Since both CAPE and vertical shear significantly impact the strength and organization of deep convection (e.g., Weisman and Klemp 1986), including these fluxes and stresses without the additional heat, moisture, and momentum sources and sinks required to preserve the quasi-steady base state would likely result in less realistic simulations and would complicate their interpretation.

Motivated by the potential difficulties discussed above and our desire to study the influence of the surface fluxes and stresses generated *internally* by the MCS on MCS structure and evolution, we include, as forcing in the model, only the portion of the fluxes and stresses that differ from that of the ambient base state. This allows the properties of the low-level inflow to the simulated squall line to remain relatively constant during the integration period, which enables us to more clearly discern the impact of MCS-induced surface fluxes and stresses on the three-dimensional evolution of the precipitation system.

The prognostic equations for the horizontal wind components (6) and (7), potential temperature (8), and water vapor (9) at the lowest model grid point are, thus,

$$\frac{\partial u}{\partial t} = -\mathbf{v}\cdot\nabla u - c_p\overline{\theta}\frac{\partial \pi}{\partial x} + \frac{\tau_{xz}}{\Delta z} - \frac{\tau_{xz}|_{t=0}}{\Delta z} \qquad (6)$$

$$\frac{\partial v}{\partial t} = -\mathbf{v}\cdot\nabla v - c_p\overline{\theta}\frac{\partial \pi}{\partial y} + \frac{\tau_{yz}}{\Delta z} - \frac{\tau_{yz}|_{t=0}}{\Delta z} \qquad (7)$$

$$\frac{\partial \theta}{\partial t} = -\mathbf{v}\cdot\nabla \theta + M_\theta + \frac{F_z^\theta}{\Delta z} - \frac{F_z^\theta|_{t=0}}{\Delta z} \qquad (8)$$

$$\frac{\partial q_v}{\partial t} = -\mathbf{v}\cdot\nabla q_v + M_{q_v} + \frac{F_z^{q_v}}{\Delta z} - \frac{F_z^{q_v}|_{t=0}}{\Delta z}. \qquad (9)$$

The final terms on the right side of (6)–(9) are the vertical divergences associated with the respective surface stresses and vertical fluxes given in (1)–(4), but at $t = 0$. These terms are simply mathematical constants representing the initial vertical fluxes and tangential stresses associated with the horizontally homogeneous ambient environment specified by the sounding (Fig. 2) and the prescribed constant SST. The additional terms on the right side of the horizontal momentum equations (6) and (7) from left to right represent the advection, horizontal perturbation pressure gradient forces, and vertical divergence of the *total* tangential stresses. The additional terms on the right side of the thermodynamic (8) and moisture (9) equations from left to right represent advection, microphysical source terms, and the *total* vertical flux divergences. Over small isolated regions within the cold pool, where ground-relative winds are particularly weak, the magnitude of the ambient surface fluxes may exceed that of the total surface fluxes [$F_z^{\theta,q_v}|_{t=0} > F_z^{\theta,q_v}(\mathbf{x}, t) > 0$]. In these rare and isolated instances, the perturbation fluxes (henceforth referred to as MCS-induced fluxes) were set to zero [$F_z^{\theta,q_v}(\mathbf{x}, t) - F_z^{\theta,q_v}|_{t=0} = 0$] to avoid unrealistic inclusion of negative fluxes as forcing in regions where the total flux is positive. Above the lowest grid point, the surface flux and stress terms [final two terms in (6)–(9)] are replaced with mixing terms in which the diffusion coefficient is determined from the subgrid-scale turbulence parameterization.

The assumption inherent in this approach is that the prescribed forcing [final terms on the right side of (6)–(9)] that allows the boundary layer in advance of the MCS to be quasi-steady would, in nature, also balance the effect of base-state fluxes and stresses in the MCS-disturbed region. Even if this assumption is not justified, the base-state fluxes and stresses that are removed are generally only a small portion of the total flux in the active deep-convective region near the MCS-leading edge (section 3c), where fluxes most directly impact deep convection. Moreover, differences between the total flux and the portion retained in this region are within the bounds of differences expected between identical quantities (e.g., the total flux) calculated with different parameterization schemes (e.g., the COARE flux algorithm vs standard bulk aerodynamic formulations), due to the uncertainty in these schemes.

d. Model initialization procedure

Deep convection is initiated by placing a 70 km × 20 km cold temperature anomaly in the center of the 540 km × 540 km horizontal domain at $t = 0$. The surface-based initial cold pool has an orientation of 330°–150° and is the aggregate of six overlapping 1.4-km-deep cylindrically shaped cold pools of radius 10 km and potential temperature deficit of 8°C from the environmental sounding. Where the cylinders overlap, the deficit remains at 8°C. During the earliest stages of model integration the collapse of this cold pool produces a scalloped gust front with preferential convergence and lifting at the intersections of the cold cylinders. Five updraft cells then form at these intersections on the downshear side of the cold pool along with cells at the line ends. After several cell lifetimes (~1.5

h), there is no longer visual evidence of the artificial initiation within the convective line.

The strong initial cold pool is an artifice used to rapidly trigger sustainable line convection in the model. This cold pool is not intended to represent typical structure and strength of convectively induced cold pools in TOGA COARE that have been found to have strengths of up to $\Delta T \geqslant -4.5°C$ (Parsons et al. 1994). The gravity current produced by its collapse, however, is intended to be representative of the observed cold pool and its associated gust front. Gravity currents produced by the release of reservoirs of cold air, and the effects of finite reservoir size, are considered in Klemp et al. (1994) and Hoult (1972), respectively. The cold pool collapse produces a gravity current of 300–500-m depth, a gust front head somewhat deeper than this, and a propagation speed slightly greater than 10 m s^{-1}, each of which are consistent with observations. The 20-km initial width of the cold reservoir is chosen so that the resulting gravity current maintains characteristics similar to those described above for ~30 min, before rapidly decaying.

In all simulations to be discussed, the cold pool weakens to a minimum intensity of $\Delta T \sim -1°C$ before intensifying as a result of model-generated convective downdrafts to strengths more typical of those observed in TOGA COARE. Both the 70-km length and the 330°–150° orientation of the prescribed cold pool were chosen to resemble the geometry of the most prominent region of observed convection during the linear band stage (Fig. 1a). As discussed earlier, the observed convective band was situated at the leading edge of a much larger cloud cluster. The onset of this leading convective band was witnessed from P-3 aircraft by one of the authors (MAL), ~70 min before the time of Fig. 1a, as a rapidly growing line of cumulus congestus 5–8 km deep over a scale similar to the length of the initiating cold pool used in the model. This sudden development with peak updrafts as large as 13.5 m s^{-1} at 2 km MSL is consistent with the release of conditional instability by strong *localized* lifting at a quasi-linear boundary (most likely a cold pool, although we have no direct evidence of this).

3. Overview of simulations and comparisons with observations

Three 6-h simulations, each initiated using the identical cold pool and otherwise horizontally homogeneous initial conditions, have been analyzed. The control simulation (CONTRL) includes the effects of ice microphysics and MCS-induced surface fluxes and stresses. The second simulation (NOFLUX) includes the effects of ice microphysics but no surface fluxes and stresses, while the third (NOICE) includes the effects of MCS-induced surface fluxes and stresses but employs the Kessler bulk microphysical parameterization that does not include ice. In the remainder of this section, we examine the general characteristics of the simulated convective systems including the precipitation, its associated low-level cold pool, and the mid-level horizontal flow structure. Comparisons with observations are included to help assess the realism of these characteristics of the simulated convective systems. Since we are most interested in oceanic influences on squall line evolution, the emphasis in the following discussion will be on results from CONTRL and NOFLUX.

a. Precipitation

The evolution of model-diagnosed radar reflectivity at 1 km MSL for CONTRL and NOFLUX appears in Fig. 3. The conversion from bulk condensate predicted in the model was accomplished using Eqs. (4) and (5) from Rutledge and Hobbs (1984), modified to account for differences in the refractive indices of water and ice as in Smith et al. (1975). The reflectivity patterns are similar through the first 3 h. By 5 h some differences are apparent: the most obvious ones being a more pronounced east–west local minimum in reflectivity rearward of the bow-shaped portion of the leading convective line and fewer convective cells along the southern flank in CONTRL. In both simulations, the transition from a quasi-linear leading edge of enhanced reflectivity to a 40–60-km bow during the period from 2 to 5 h near the center of the larger-scale precipitation arc (Fig. 3) strongly resembles the observed evolution (Fig. 1). During this transition, elongated bands of enhanced reflectivity ($Z > 38$ dBZ) oriented approximately normal to the leading edge convection develop rearward of the southern portion of the bow-shaped segment, also resembling observations (cf. Figs. 1 and 3). The transverse band present at 5 h in CONTRL (Fig. 3) is particularly prominent due to the reflectivity minimum to its north. A similar notch of weak reflectivity is found in the radar data at 2219 UTC (Fig. 1c).

While the evolution from linear to bow-stage is well represented, the continued strength of the bow-shaped leading convective band (particularly in CONTRL) contrasts significantly with observations. However, the decay of the observed rainband ~1 h after evolving into the bow-shaped stage (Fig. 1) coincided with its approach to and movement over the Russell Islands and Guadalcanal. By this time aircraft soundings, obtained in advance of the squall line, indicate changes in the flow within the lowest few hundred meters from $(u, v) = (1, -7)$ to $(8, -2)$ that result in a substantial reduction in inflow vertical shear. This change in the actual ambient low-level flow may contribute to differences in the later stages of observed and simulated MCS evolution.

The slightly smaller scale of the simulated precipitation pattern constitutes a second difference between simulations and observations. We believe that this is largely an artifact of the size of the prescribed initial

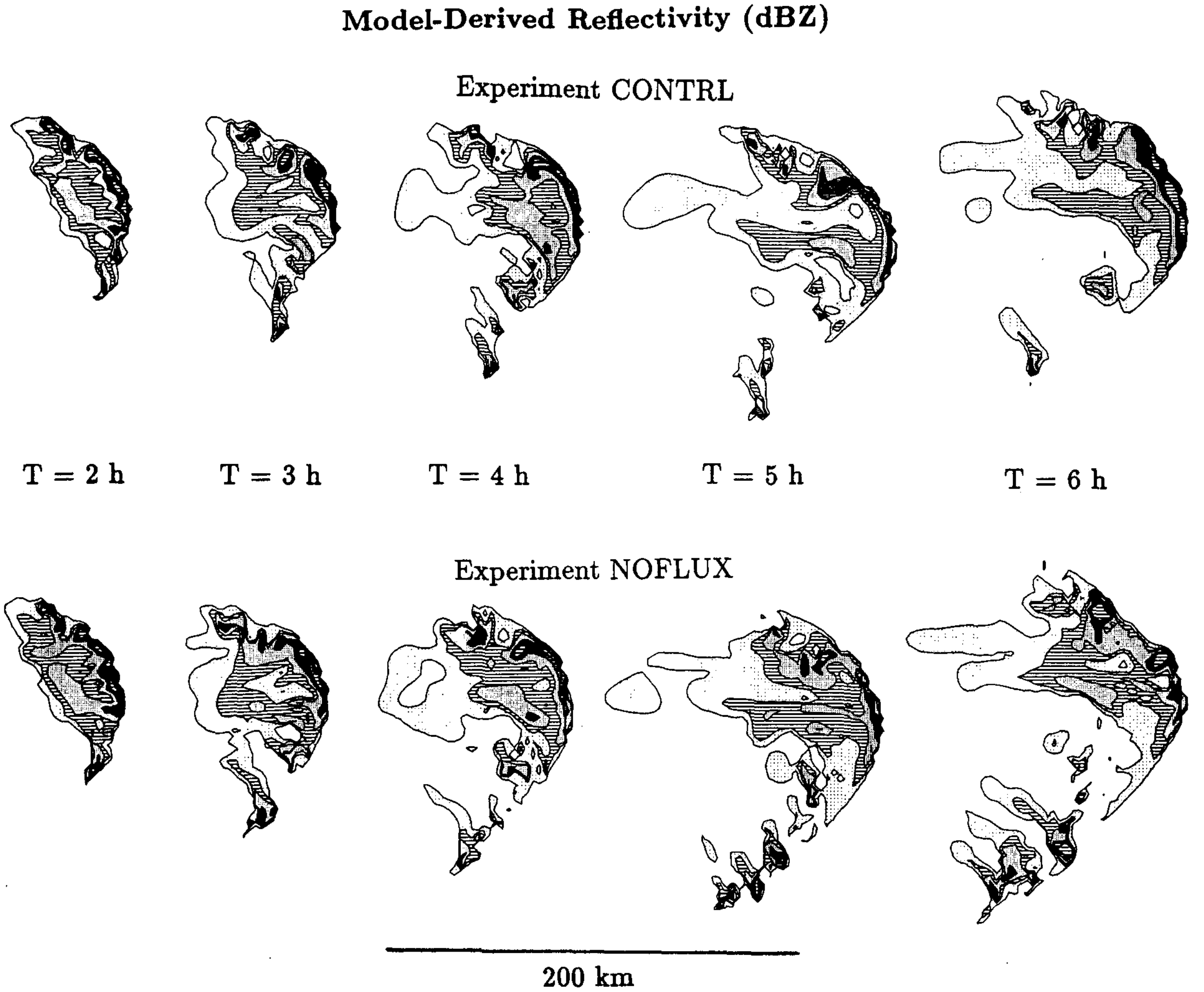

FIG. 3. Evolution of simulated radar reflectivity at 1 km MSL estimated from model-predicted bulk microphysical variables for experiments CONTRL (top) and NOFLUX (bottom). Shading intervals are dots (15–30 dBZ), lines (30–38 dBZ), dense dots (38–45 dBZ), dense lines (45–50 dBZ), and thin lines (50+ dBZ).

cold pool that was intended to represent the scale of forcing responsible for the initiation of the linear band of enhanced radar reflectivity (Fig. 1a), which constitutes only a portion of the observed MCS. Finally, the cellular development along the far southern flank of the simulated systems with lesser amounts of stratiform precipitation is not supported by the available observations (Fig. 1). In this respect experiment CONTRL, in which these cells are less extensive and diminish with time (Fig. 3), is more consistent with observations than is experiment NOFLUX.

b. Midlevel flow structure

In the foregoing discussion, we noted that the transition of the leading convective zone from a linear to bow-shaped structure during the period from 2 to 4 h occurs in both CONTRL and NOFLUX (Fig. 3). In both cases this evolution is strongly associated with changes in the midlevel flow structure (Fig. 4). At 2 h (Figs. 4a,d) small-scale (~5–10 km) counter-rotating vortex circulations are evident at the ends of the quasi-linear segment of continuous midlevel updraft. By 4 h (Figs. 4b,e), these circulations have increased in scale and are associated with the evolution to a bow-shaped updraft, a dramatic increase in maximum system-relative rear inflow from 4 to 12 m s^{-1}, and a subsequent decrease in estimated reflectivity within the zone of strong rear inflow by 5 h (cf. Fig. 3). The maximum ground-relative wind speeds of 24 m s^{-1} during the mature phase of the bow-shaped leading convective line far exceed those at any level in the environmental wind profile (Fig. 2). The maximum rear inflow and system propagation speed (10–14 m s^{-1}) of the simulated systems are within 1–2 m s^{-1} of observed values (Jorgensen

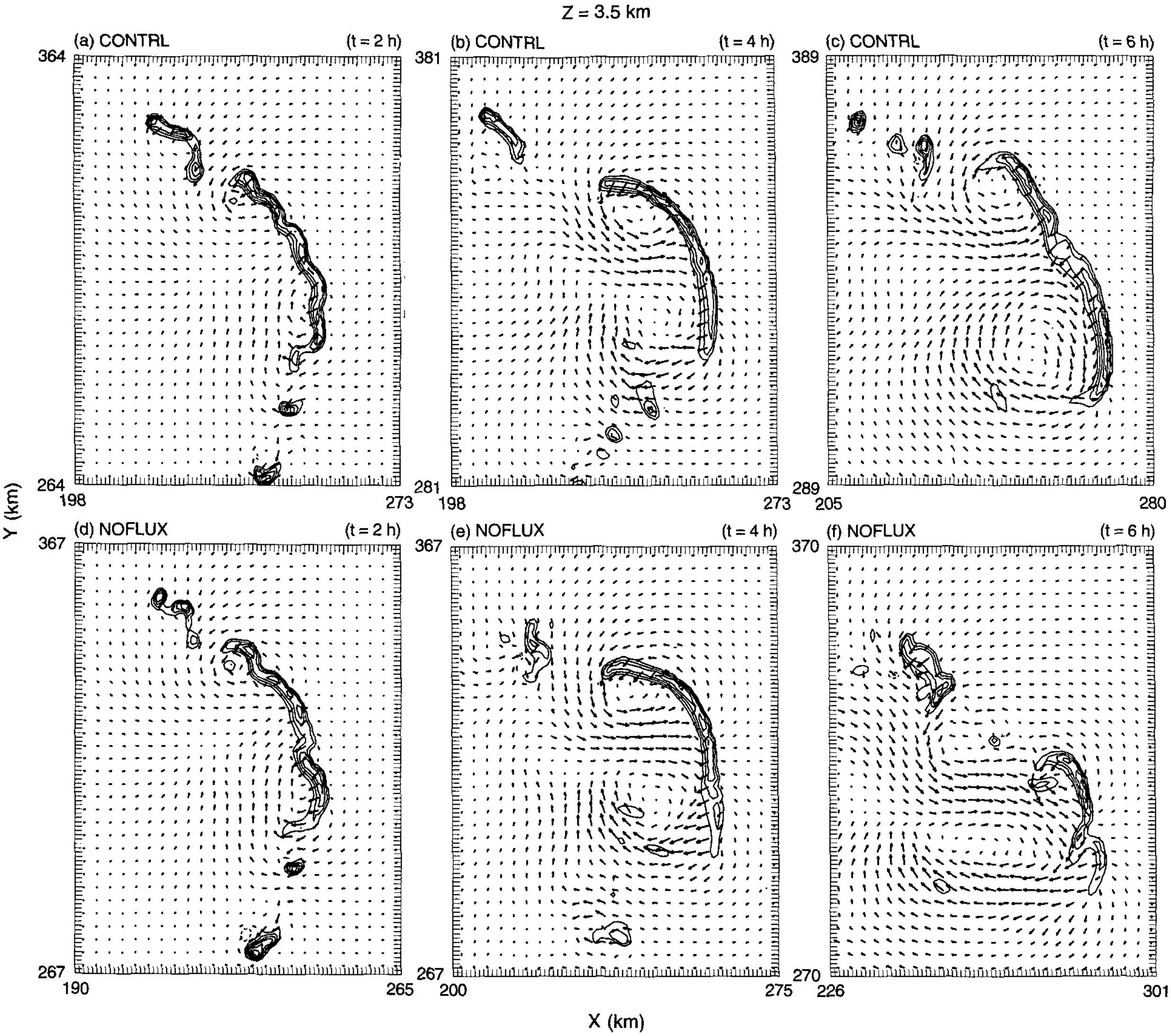

FIG. 4. Simulated vertical velocity at 3.5 km MSL in intervals of 2 m s^{-1} (positive values solid, negative values dashed, zero line omitted) and approximate system-relative wind vectors (vector length of 1 grid box is equivalent to 4 m s^{-1}) at 3.5 km MSL (vectors plotted every third grid point) for experiment CONTRL at (a) 2 h, (b) 4 h, and (c) 6 h, and for experiment NOFLUX at (d) 2 h, (e) 4 h, and (f) 6 h.

et al. 1995), which results in similar ground-relative maximum winds. The increase in rear inflow is consistent with the rear-inflow enhancement between two counterrotating vortices described by Weisman (1993) for midlatitude bow-echo MCSs.

By 6 h differences between CONTRL and NOFLUX are evident in the midlevel updraft and horizontal flow structure. In NOFLUX (Fig. 4f), the original mesoscale vortices are situated well to the rear of the leading edge. This development is concurrent with an increase in the propagation speed of the leading edge from 11 m s^{-1} at 4 h to 14 m s^{-1} by 6 h. The midlevel updraft weakens substantially in the vicinity of the original northern vortex. Convection is still relatively strong farther to the south and a new counterclockwise-rotating vortex is beginning to form near the new position of the line end. In contrast, a continuous updraft is still present at 6 h in CONTRL (Fig. 4c), and the original mesoscale vortices are still closely tied to the ends of this updraft, although the updraft itself is beginning to weaken near the center of the leading edge.

The observed and simulated (experiment CONTRL) convective systems share several midlevel (z = 4.5 km) features during their respective evolutions. At 4 h of simulation, similarities include the bow-shaped leading edge of the precipitation pattern and the ~30-km horizontal scale of the northern vortex (Fig. 5). At this height, strong horizontal shear occurs within the strong front-to-rear flow at the southern end but closed circulation is less pronounced than with the northern vortex (Figs. 5a,b). The typical maximum vertical vorticity (0.004–0.007 s^{-1}) and depth (closed circulation from 0.5 to 5.5 km MSL) of the northern vortex was generally greater than the southern vortex in both the simulations and observations. Differences between observations and the simulation at this elevation include the slightly larger scale of the observed bow (60 vs 45 km) and its less intense radar reflectivity.[2]

c. *Cold pool and surface fluxes*

The evolution of the simulated squall line from the quasi-linear to bow-shaped stage is accompanied by growth in the scale and intensity of cooling and drying (absolute humidity) at low levels behind the leading edge (Figs. 6, 7). The lateral spreading of the cold pool is consistent with both the rapid propagation and lengthening of the leading convective line. Comparison of CONTRL (Figs. 6b, 7b) with NOFLUX (Figs. 6d, 7d) reveals that inclusion of the MCS-induced fluxes generally decreases the strength, but more dramatically the areal extent, of the cooling and drying associated with deep convection by 5 h. The potential temperature and moisture deficits near the leading edge of the central portion of the squall line, where the cold pool is strongest, are similar in CONTRL and NOFLUX despite strong MCS-induced fluxes in this region of CONTRL (Fig. 8). In this zone, cold convective downdrafts replenish the cold air mass faster than fluxes are able to warm and moisten it. While fluxes are not nearly as strong farther to the rear and also along the northern and far southern flanks of the leading edge, they are generally less opposed by strong penetrative downdrafts that transport low θ_e air from above.

The maximum MCS-induced sensible heat and moisture fluxes at 5 h in experiment CONTRL (Fig. 8) are situated slightly southward of the regions of maximum θ and q_v deficits (Figs. 6b, 7b) and coincide with the strongest ground-relative winds. The magnitudes of the MCS-induced fluxes calculated from the in situ aircraft-based flux estimates reported in LeMone et al. (1995)[3] fall within the range of simulated values in Fig. 8. The maximum values of MCS-induced fluxes in CONTRL found near the leading edge greatly exceed the ambient fluxes (Fig. 8). Rearward of this zone of active deep convection, the winds are generally weaker and the ambient fluxes thus constitute a much larger percentage of the total flux. In this region, referred to as the "convective wake" by Barnes and Garstang (1982), our flux formulation that does not include the ambient fluxes is expected to most noticeably underestimate the influence of the total fluxes and the rate of boundary layer recovery.

(a) Doppler Radar Observations

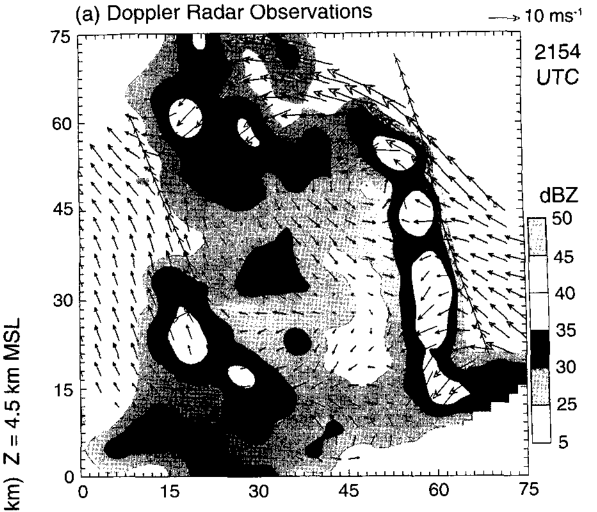

(b) Experiment CONTRL

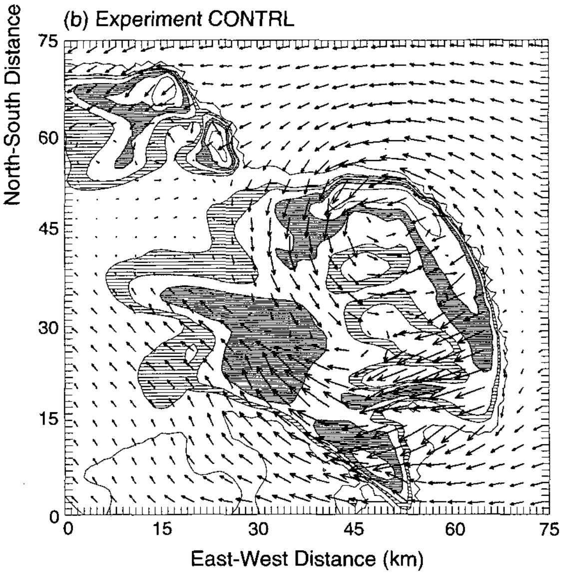

FIG. 5. (a) Dual-Doppler radar analysis constructed from P-3 aircraft data of system-relative flow and reflectivity (dBZ) at 4.5 km MSL for a portion of the southern convective segment depicted in Fig. 1 at 2148 UTC 22 February 1993, and (b) reflectivity [5 (dots), 25 (lines), 30 (dense dots), 35 (dense lines), 40 (unshaded), and 45 (dots) dBZ thresholds] estimated from model-predicted bulk microphysical quantities with approximate system-relative flow vectors at 4.5 km MSL for the bow-shaped region of experiment CONTRL at 4 h. The scale of the system-relative flow vectors for the simulations is identical to that of the Doppler radar observations.

As noted in section 3a, the most substantial differences in the precipitation pattern between NOFLUX

---

[2] A combination of factors likely influence the discrepancies between radar and model-estimated reflectivity including slightly greater updraft strength in the model at this time, attenuation effects on radar reflectivity by heavy precipitation at X-band wavelengths, and limitations inherent in an assumed precipitation size distribution specified in the bulk microphysical parameterization (e.g., Smith et al. 1975).

[3] The calculations of fluxes from observations utilized flight level (158 m MSL) winds and employed an early version of the COARE flux algorithm (Fairall et al. 1996). In the simulations, we calculate fluxes using (1)–(5) at the lowest model grid point (50 m MSL).

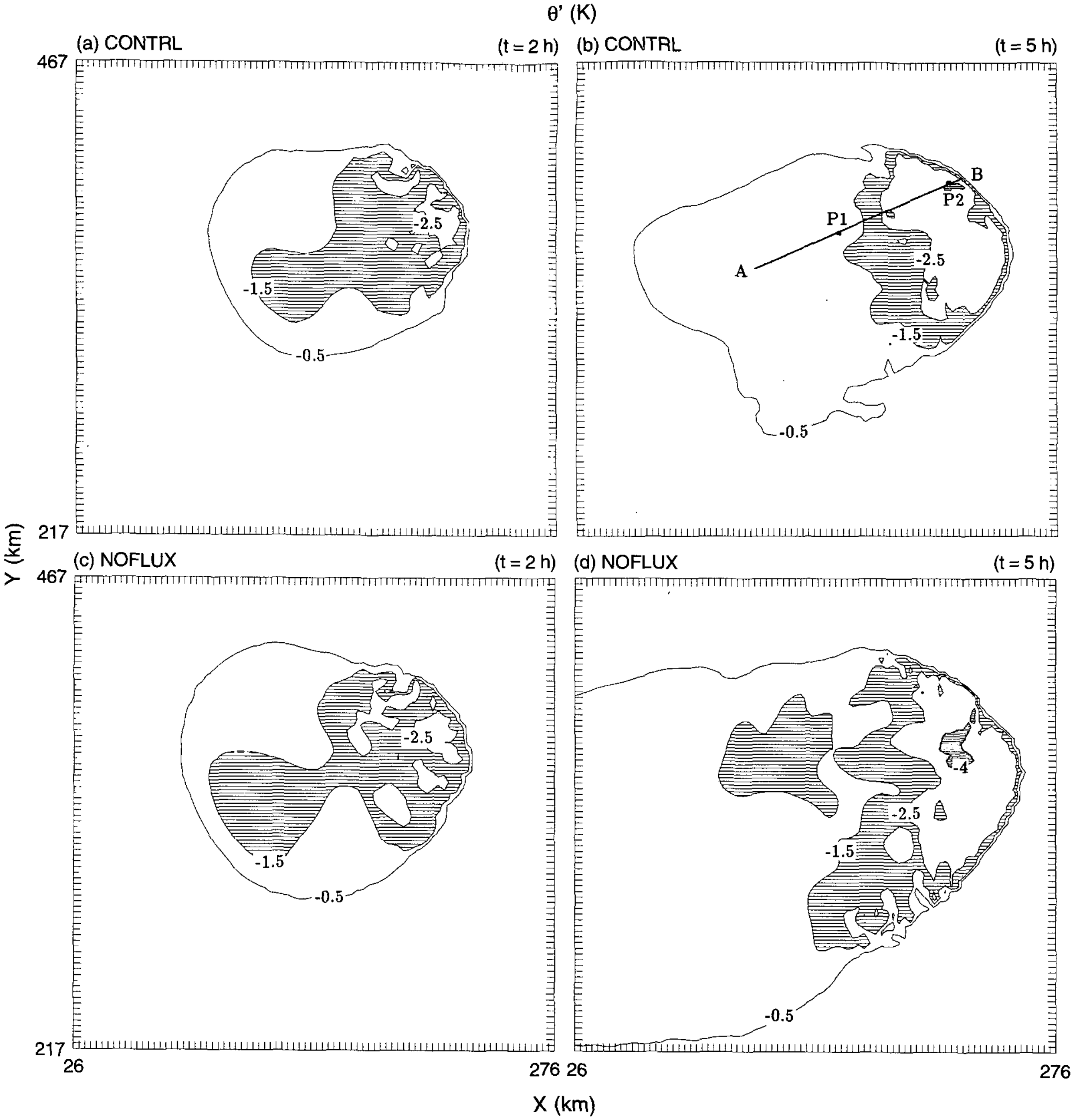

FIG. 6. Potential temperature perturbations from initial conditions at 158 m MSL for experiment CONTRL at (a) 2 h and (b) 5 h and for experiment NOFLUX at (c) 2 h and (d) 5 h. Shading intervals are −0.5° to −1.5°C (dots), −1.5° to −2.5°C (lines), −2.5° to −4.0°C (dense dots), and ≤ −4.0°C (dense lines).

and CONTRL occur along the far southern flank (Fig. 3). In Fig. 9 we find that the more widespread single-cell convection in NOFLUX, which is less consistent with observations, is associated with a stronger gradient of surface potential temperature at the leading edge of the cold pool. In this relatively weak portion of the leading-edge cold pool, the percentage differences in temperature and moisture deficits between CONTRL and NOFLUX are largest. In cases where cold pools are especially weak or shallow, the tendency for the surface fluxes acting over an extended period of time to further weaken the cold pool may result in its subsequent inability to help support deep convection. The stronger potential temperature gradient along the far

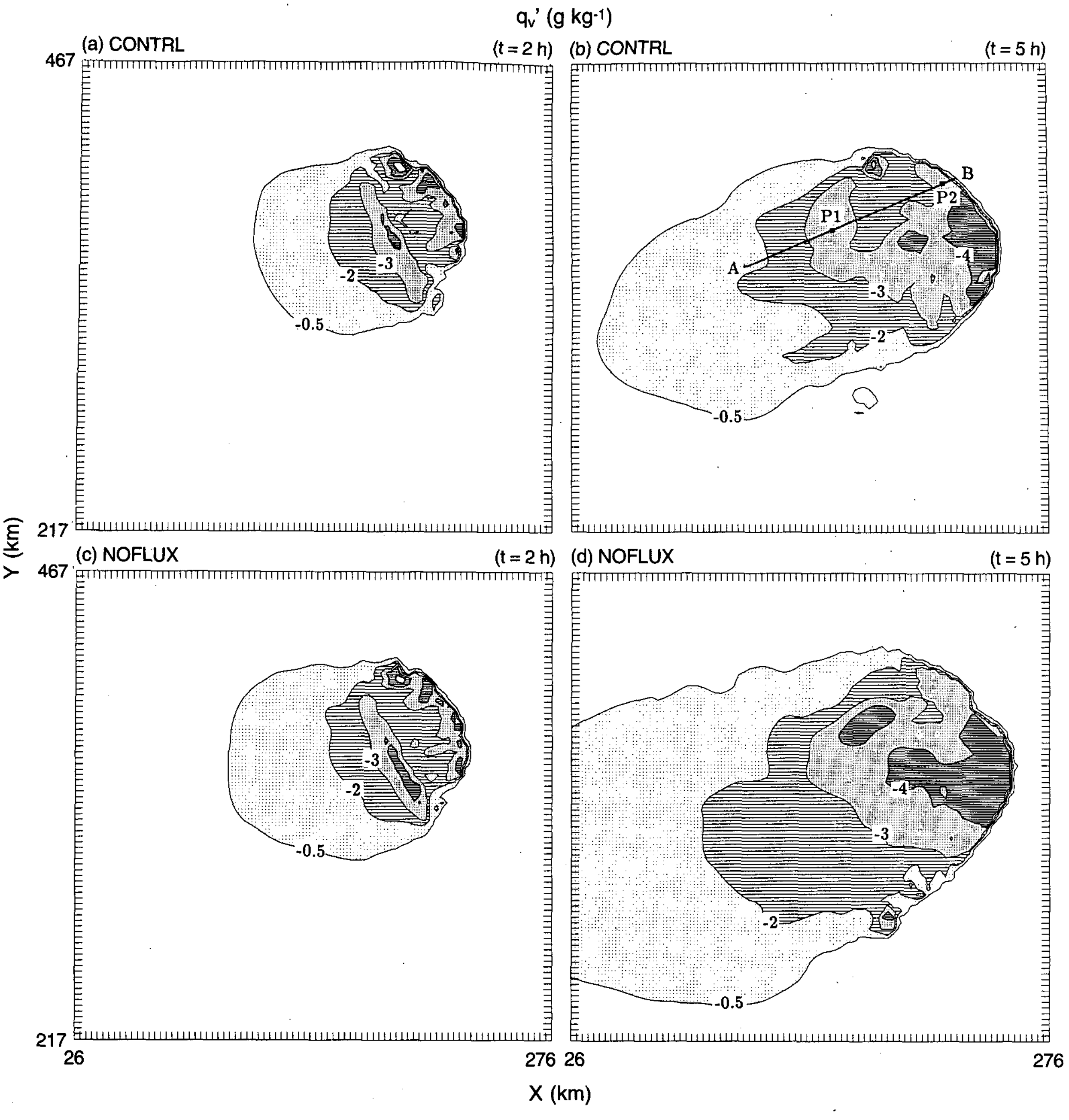

FIG. 7. Water vapor mixing ratio perturbations from initial conditions at 158 m MSL for experiment CONTRL at (a) 2 h and (b) 5 h, and for experiment NOFLUX at (c) 2 h and (d) 5 h. Shading intervals are −0.5 to −2.0 g kg^{-1} (dots), −2.0 to −3.0 g kg^{-1} (lines), −3.0 to −4.0 g kg^{-1} (dense dots), and −4.0 to −5.0 g kg^{-1} (dense lines).

southern flank in NOFLUX results from a feedback process in which the absence of fluxes leads to a more intense cold pool that helps sustain deep convection, which further intensifies the cold pool.

Although aircraft observations do not provide the full spatial distribution and evolution of θ and q_v within the cold pool, comparison of available data with model results reveals similar mesoscale characteristics. In Fig. 10 we compare time series of measurements taken along aircraft legs flown from the rear toward the front of the MCS at an altitude of 158 m MSL with values from experiment CONTRL along line *B–A* (Figs. 6b, 7b). These two transects are at identical elevation and in a similar position relative to mesoscale precipitation

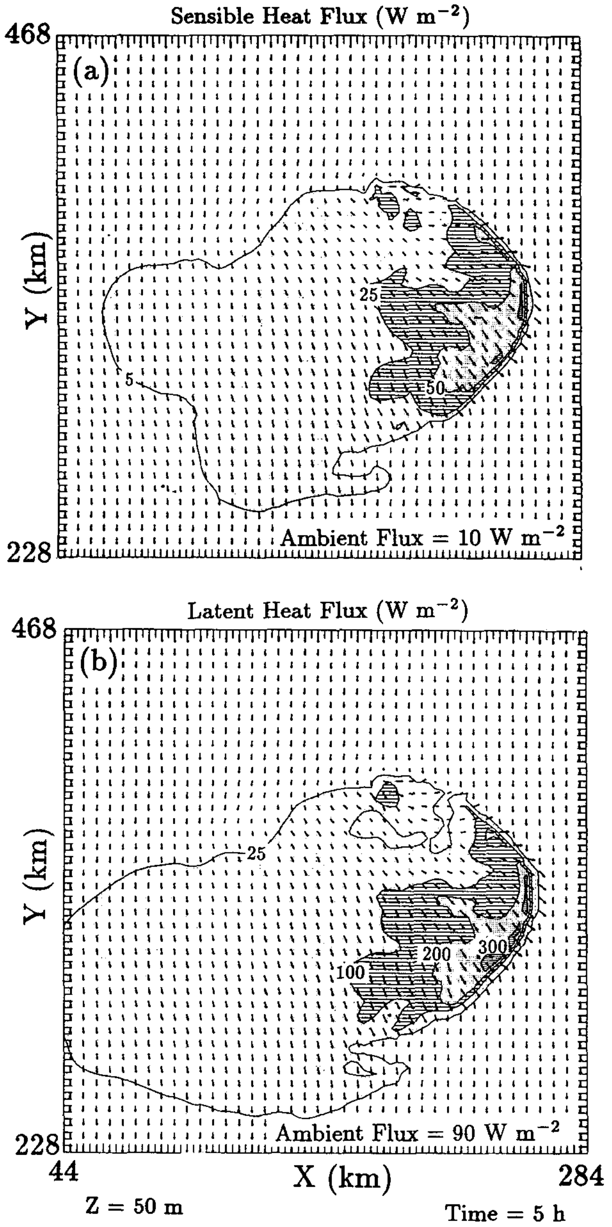

FIG. 8. Simulated ground-relative winds (plotted every 6 km) overlaid on (a) perturbation (MCS-induced) sensible heat fluxes with shadings of 5–25 W m^{-2} (dots), 25–50 W m^{-2} (lines), 50–75 W m^{-2} (dense dots), and ≥75 W m^{-2} (dense lines), and with (b) perturbation (MCS-induced) latent heat fluxes with shadings of 25–100 W m^{-2} (dots), 100–200 W m^{-2} (lines), 200–300 W m^{-2} (dense dots), and ≥300 W m^{-2} (dense lines) at 50 m MSL for experiment CONTRL at 5 h.

features (cf. LeMone et al. 1995; their Fig. 1). In both cases the coolest conditions are located within 20 km of the leading edge of the precipitation system and are followed by a rapid recovery to within 1° to 1.5°C of the ambient values ~60 km from the leading edge (Fig. 10a). Further warming then proceeds more slowly in both the model and observations. A secondary local minimum in q_v well to the rear of the coldest temperatures is found in both the simulation (in the vicinity of P1 of Fig. 7b) and observations. This local minimum is located 20 km farther to the rear in the observations and is preceded by a more complete moistening (Fig. 10b).

A model sounding (Fig. 11, solid), taken within light stratiform rain at P1 along line A–B of Fig. 7b, reveals a 40-mb-deep (~400 m) surface cold pool with warm and dry conditions relative to the initial sounding

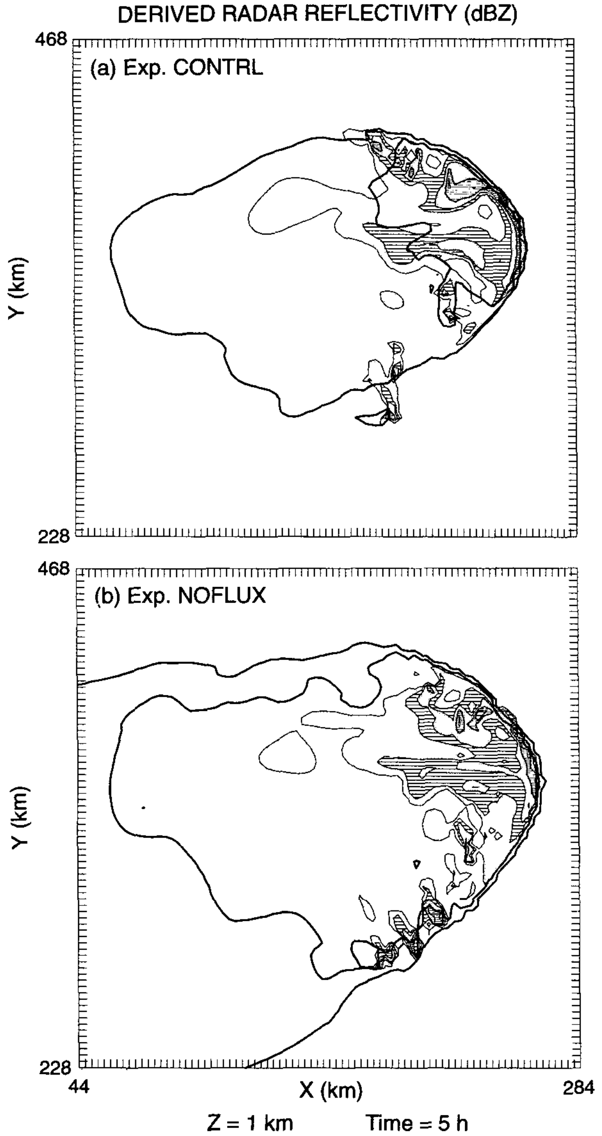

FIG. 9. Selected −0.5°C and −2.0°C contours of surface potential temperature perturbations emphasizing the cold pool boundary with radar reflectivity derived from model-predicted bulk microphysical variables (shadings as in Fig. 3) at 1 km MSL for experiments (a) CONTRL and (b) NOFLUX at 5 h.

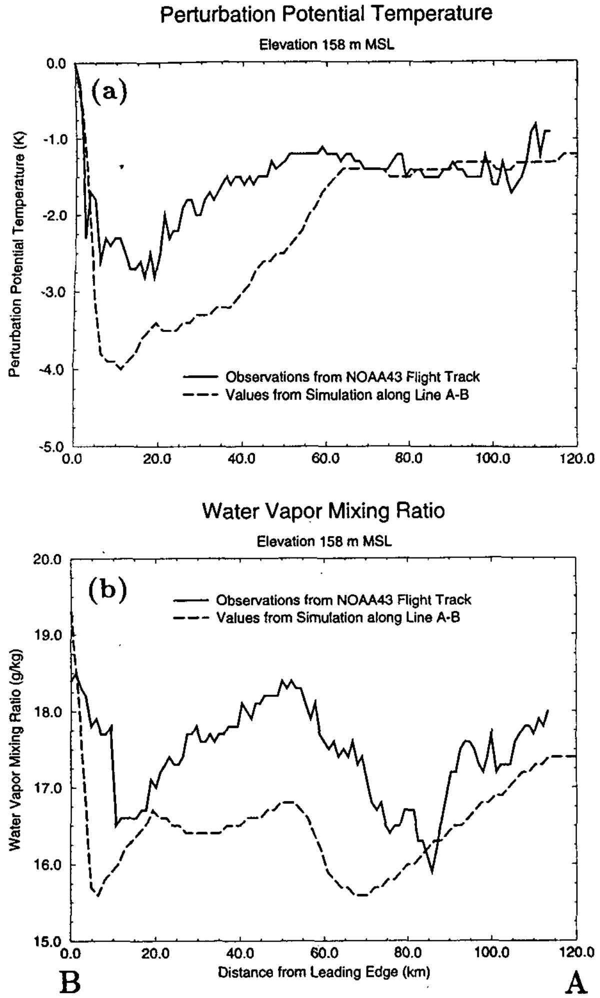

FIG. 10. (a) Potential temperature perturbations from ambient values and (b) water vapor mixing ratio at 158 m MSL from the front toward the rear of the squall line observed from P-3 aircraft during a flight leg from 2337 to 2356 UTC 22 Feb 1993 (solid) whose position within the observed MCS is illustrated in LeMone et al. (1995; Fig. 1) and from experiment CONTRL at 5 h along line *B–A* of Figs. 6b, 7b (dashed).

(Fig. 11; dashed) located above. The warm and dry conditions above a shallow cold pool are characteristic of mesoscale descent (Zipser 1977; Johnson and Nicholls 1983) induced by stratiform precipitation processes (Brown 1979; Leary and Houze 1979a,b). In contrast, a model sounding (Fig. 11, dotted) taken at P2 along line A–B of Fig. 7b, within intense convective rainfall near the leading edge, is cold with respect to the initial sounding and remained nearly saturated below cloud base at 900 mb (~1 km MSL). Observations presented in LeMone et al. (1995) reveal similar variability in the vertical structure of the subcloud layer rearward of the squall line during its later stages, except that the boundary layer is warmer and more moist immediately rearward of the leading edge of convection (Fig. 10).

The 1° to 1.5°C cooler (Fig. 10a) and 1 g kg^{-1} drier (Fig. 10b) than observed near-surface conditions immediately behind the leading edge in the simulation may result from many different factors. First, the observations from Fig. 10 were collected after the squall line had weakened. At the corresponding later bow stage in the simulation, the squall line is still relatively intense. Second, exclusion of the ambient fluxes in CONTRL may be relatively significant along this northern portion of the squall line, where the MCS-induced fluxes are weak (Fig. 8). Third, time-dependent back trajectories from near the surface at the leading edge of the simulated cold pool (presented in a future paper) show that this air originates in the rear-inflow current at 2 km MSL or slightly above, where the environmental θ_e is lowest. If the observed local θ_e minimum near the leading edge of the cold pool has a similar origin from the rear, we would expect a somewhat higher θ_e than simulated, since comparison of vertical cross sections (presented later in section 4; Fig. 14) suggest that the observed rear-inflow originates at a slightly lower level, where environmental θ_e is higher. Fourth, additional limitations in the model, including uncertainties in the parameterization of subgrid-scale turbulence and vertical resolution insufficient to resolve detailed boundary-layer structure and processes, may influence results. Finally, possible differences in the position and timing of the observational and model transects relative to transient convective cells will influence the comparison. The similarity in the mesoscale trends of θ and q_v between experiment CONTRL and the observations lends confidence that the simulation is a reasonable analog of the observed system. However, the above factors dictate that quantitative aspects of the comparison be interpreted with caution.

4. Vertical structure of the simulated MCS

A distinct characteristic of the observed squall line was the pronounced rearward tilt (relative to the direction of squall line motion) of convective updrafts during its linear stage (Jorgensen et al. 1995). The evolution of the low- (1.5 km) and midlevel (6 km) vertical motions for all three simulations (CONTRL, NOFLUX, and NOICE) from 2 to 4 h are displayed in Fig. 12. At 2 h each simulation evinces a rearward tilt (inferred from the horizontal separation between the 1.5- and 6-km updrafts) over a ~60-km region of the line centered on a strong (5–8 m s^{-1}) and continuous low-level updraft. While most aspects of the updraft structure during the 2-h period are similar in CONTRL and NOFLUX, (Figs. 12a,b) significant differences are apparent in NOICE (Fig. 12c). These differences include a more substantial rearward tilt at 2 h and a subsequent more rapid evolution away from a linear midlevel updraft pattern. For instance at 3 h, both CONTRL and

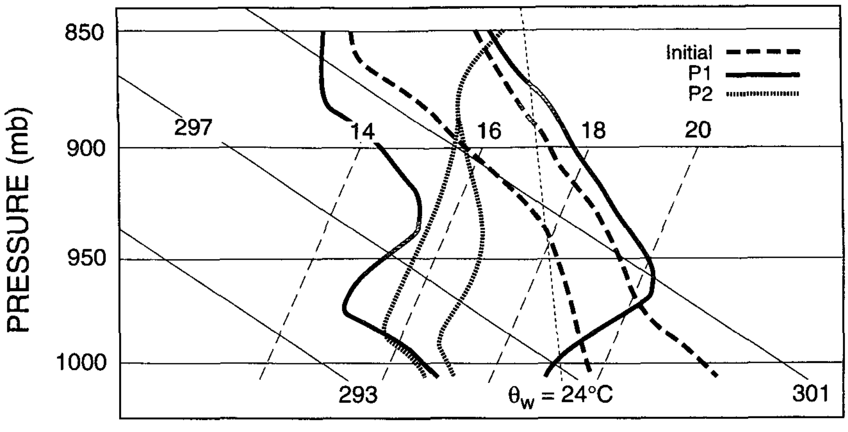

FIG. 11. Skew T–ln$P$ diagram of temperature and dewpoint curves for the initial conditions (dashed) and at 5 h for points P1 (solid) and P2 (dotted) along line A–B in Figs. 6b and 7b of experiment CONTRL.

NOFLUX still possess a quasi-linear 40–50 km long segment of continuous midlevel updraft near the center of the precipitation system, whereas, the midlevel updraft in NOICE is more three-dimensional by this time.

In each of the simulations the vertical structure becomes more difficult to classify with time due to the pronounced along-line variability that develops during the later stages. For example, the degree of upshear tilt in both CONTRL and NOFLUX is fairly uniform near the center portion of the squall line at 2 and 3 h but is quite variable by 4 h (Figs. 12a,b). We can, however, characterize the vertical structure during the more linear stage (when an average structure is more meaningful) by averaging along 40-km segments (enclosed by the short brackets in Fig. 12) that are approximately parallel to the central portion of the leading edge of the convective band. It should be kept in mind that the forthcoming analyses of thermodynamic and kinematic quantities are only representative of the vertical structure over a limited region of the simulated squall line during its early stages.

The model-estimated radar reflectivity for the line-average of CONTRL at 3 h (Fig. 13a) exhibits several features commonly found in tropical squall lines. There is a convective region 25-km wide consisting of a low-level reflectivity maximum near the leading edge with a rapid reflectivity decrease above the melting level (~5 km MSL). The mean slope of the 10-dBZ contour in the convective region, above the vertically erect leading edge that extends to 5 km, is approximately 25° from the horizontal, consistent with the findings of LeMone et al. (1984b) for GATE convective lines. Significant precipitation from the anvil cloud reaches the ground up to 65 km behind the leading edge and then extends rearward aloft to 100 km from the leading edge.

Examination of the bulk mixing ratios from the various hydrometeor classes aids in the interpretation of the model-estimated reflectivity pattern. Comparison of Fig. 13a with Figs. 13b–d reveals that the shallow reflectivity maximum associated with the strong leading edge updraft (Fig. 12) results almost entirely from warm-rain processes. The deeper reflectivity feature 15 km to its rear (Fig. 13a) is composed of both graupel (Fig. 13c) and rain (Fig. 13b) with small amounts of snow near its summit (Fig. 13d). Snow and small amounts of graupel are present in the portion of the anvil adjacent to the convective region, while the portion of the anvil where precipitation remains aloft is composed entirely of snow. McCumber et al. (1991) point out that it is not likely that significant amounts of graupel actually exist in the stratiform region of tropical squall lines but that the fall speeds of these particles as parameterized in the Rutledge and Hobbs scheme are similar to those of large aggregates of snow that are predominant in observed systems.

A substantial rearward tilt of the convective updraft suggested earlier in Fig. 12a is confirmed in the line-averaged vertical motion (Fig. 14b). Distinct maxima consist of a 5–6 m s^{-1} updraft from z = 1.5 to 4 km near the leading edge and a 2–3 m s^{-1} updraft from z = 9 to 12 km, 15–20 km to the rear. The observed line-averaged vertical velocity (Fig. 14a), also from the linear stage, similarly reveals the double-peaked updraft structure. The altitudes of the observed low-level and secondary updraft maxima, their horizontal separation, and the tilt of the convective updraft region closely resemble that of experiment CONTRL. A midtropospheric minimum in vertical velocity rearward of a strong low-level updraft has been observed in other large tropical squall lines occurring in lower-tropospheric jet environments (e.g., Chong et al. 1987).

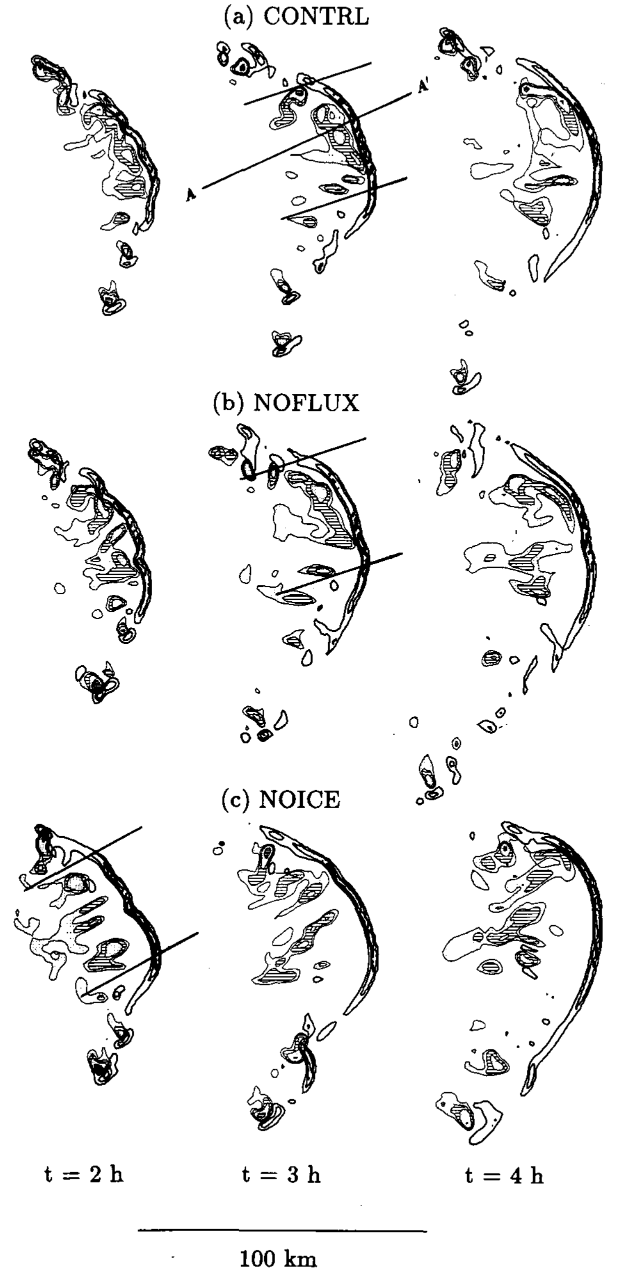

FIG. 12. Evolution of simulated vertical velocity at 1.5 km MSL (1, 4, and 7 m s^{-1} solid contour intervals) and at 6 km MSL indicated by shading with 1 to 2.5 m s^{-1} (dots), 2.5 to 5 m s^{-1} (lines), 5 to 10 m s^{-1} (dense dots), and ≥10 m s^{-1} (dense lines) intervals for (a) experiment CONTRL, (b) experiment NOFLUX, and (c) experiment NOICE. The short brackets enclose the averaging domain in the along-line direction for vertical cross sections displayed in subsequent figures. Line *AA′* denotes position of the vertical cross section in Fig. 15.

While the observed strength of the low-level updraft is similar, the secondary updraft maximum ~20 km to the rear is about three times as strong as its simulated counterpart. Transects through the deeper individual simulated cells (e.g., Fig. 15), however, exhibit maximum updrafts in the upper troposphere that are nearly as strong as those of individual observed updraft cells (Jorgensen et al. 1994; their Fig. 5). The greater strength of the observed line-averaged upward motion in the upper troposphere is due primarily to a larger number of cells and stronger upward motion between cells. The observed line-averaged updraft is broader than its simulated counterpart (Fig. 14). The greater width, which is most pronounced at low levels near the gust front results, in large part, from spatial filtering of the radar data. Convective-scale downdrafts of 1–2 m s^{-1} in the middle and lower troposphere that are not resolved in the line average, are evident in two distinct locations: immediately behind the shallow leading-edge updraft and beneath the secondary upper-tropospheric updraft (Fig. 15). Outside of the line-averaging area, updrafts along the northern flank of the simulated line (not shown) were generally stronger in the upper troposphere and did not exhibit a midtropospheric minimum.

Further examination of the line average of experiment CONTRL (Fig. 16a) reveals a broad region of weaker vertical motion extending rearward from the active convection zone. A sloping *mesoscale* updraft (0.1–1 m s^{-1}) denoted by the thick solid line coincides with a large portion of the anvil reflectivity region (cf. Fig. 13a). A mesoscale downdraft (-1 to -0.1 m s^{-1}) denoted by the thick dashed line is present below the mesoscale updraft and is deepest within the stratiform precipitation region, where it extends from just above the surface to near the melting level. During the linear stage of the MCS, the majority of the mesoscale downdraft is associated with weak system-relative rear inflow while the mesoscale updraft is fed by strong front-to-rear flow (Fig. 16b).

The perturbation potential temperature field (Fig. 16c) shows that the top of the mesoscale downdraft is cold relative to initial (ambient) conditions, consistent with melting and evaporation beneath the anvil cloud. In contrast, the major core of the mesoscale downdraft below the melting level from 1 to 4 km MSL is warm relative to initial conditions. In this zone, exemplified by the model sounding (Fig. 11, solid lines) in the vicinity of the more rearward near-surface q_v minimum, subsidence-induced adiabatic warming exceeds cooling by evaporation. Within the convective updraft region, the largest line-averaged positive temperature perturbations (Fig. 16a) occur in the region of strongest front-to-rear flow (Fig. 16b) in the middle troposphere extending rearward from the leading edge updraft (Fig. 16a). A separate weaker local maximum present in the upper troposphere is nearly collocated with a region of snow production (Fig. 13d).

The most pronounced feature of the perturbation pressure field (Fig. 16d) is a 25 to 30 km scale mesolow of -0.5-mb maximum intensity situated di-

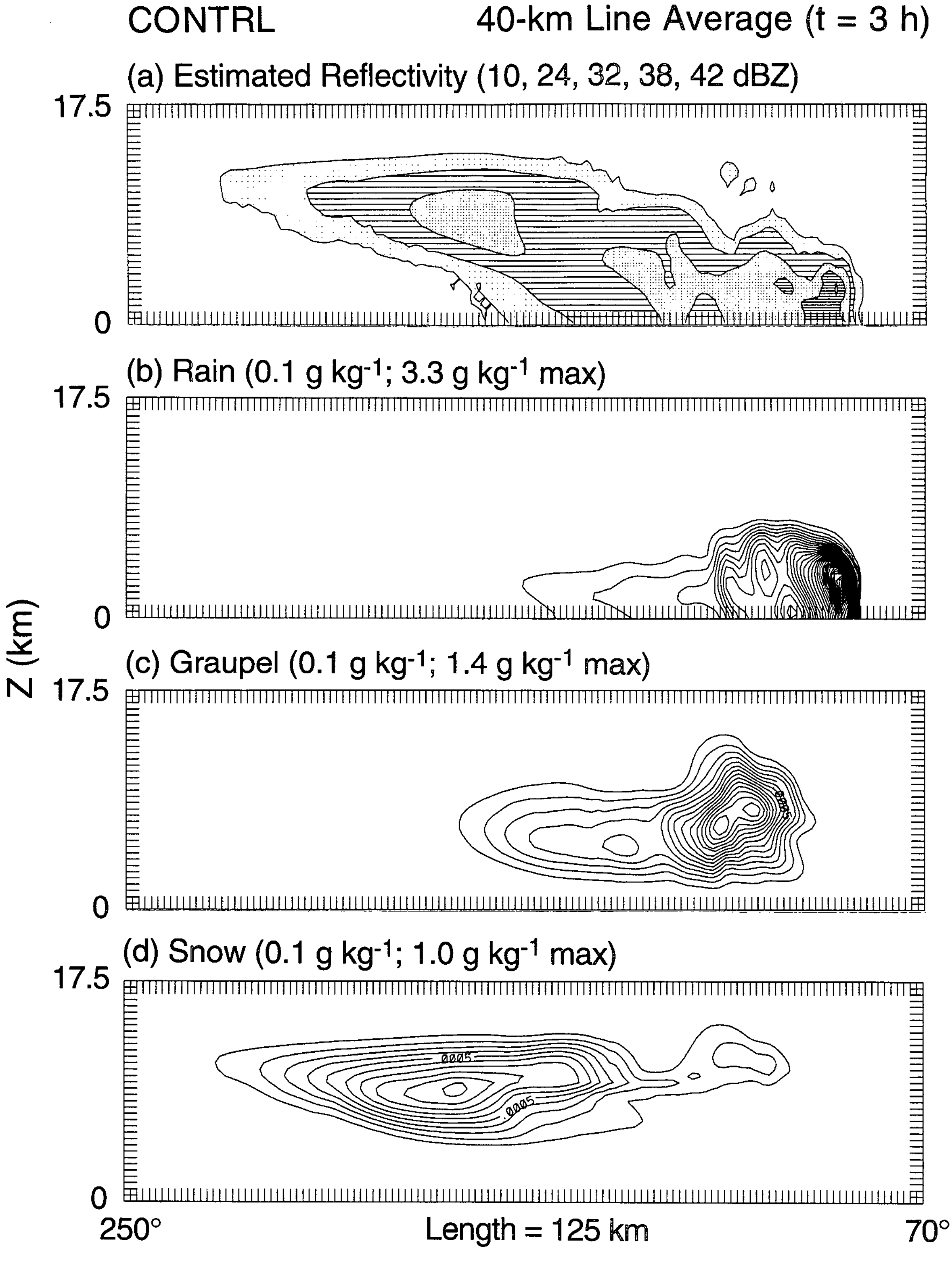

FIG. 13. Vertical cross sections from 40-km averages taken along azimuth 340°–160° (averaging region enclosed by brackets in Fig. 12a) approximately parallel to the center portion of the leading edge updraft at 3 h in experiment CONTRL of (a) radar reflectivity (10-, 24-, 32-, 38-, and 42-dBZ thresholds) estimated from model-predicted bulk microphysical variables, (b) rain (0.1 g kg^{-1} contour intervals), (c) graupel (0.1 g kg^{-1} contour intervals), and (d) snow (0.1 g kg^{-1} contour intervals). In each panel the vertical scale is exaggerated 2:1.

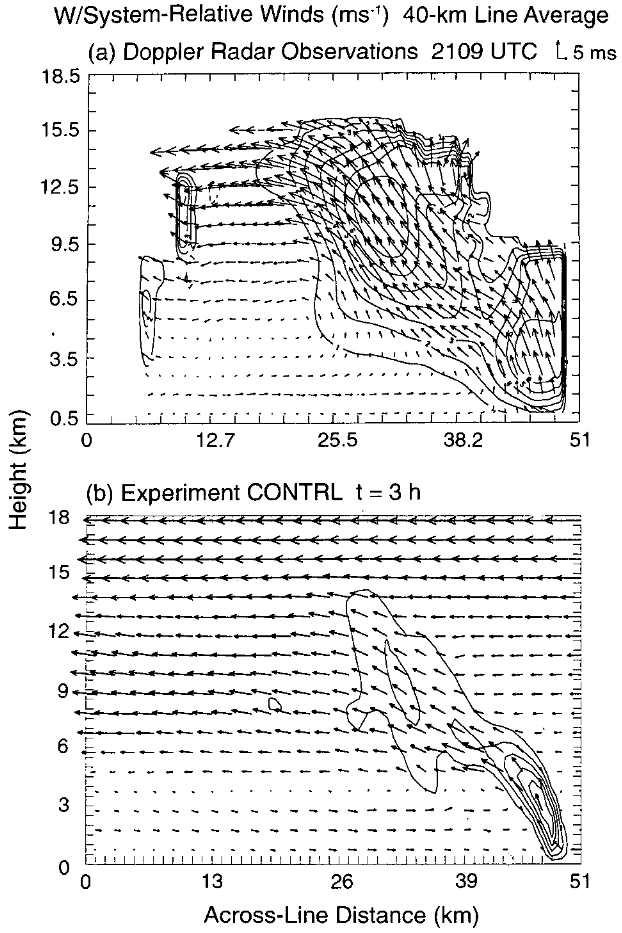

FIG. 14. Vertical velocity (1 m s^{-1} contour intervals; positive values solid, negative values dashed) and approximate system-relative flow constructed from 40-km averages approximately parallel to the leading edge updraft (a) from Doppler radar observations during the linear stage of the squall line (2109 UTC 22 Feb 1993) and (b) for the portion of experiment CONTRL enclosed by the brackets in Fig. 12a. In each panel the vertical scale is exaggerated 2:1.

rectly underneath the sloping updraft. Its position is consistent with the vertical gradients of buoyancy that result from the juxtaposition of warming from condensation and freezing in the convective updraft with cooling from evaporation in the subcloud air mass below (Fig. 16c). This feature is common to convective lines that possess a significant upshear tilt (e.g., LeMone et al. 1984a). Beneath the mesolow a shallow 0.5–1-km-deep surface mesohigh of maximum intensity 0.8 mb is associated with the subcloud cold air mass.

While the basic features of the line-averaged cross section of NOFLUX are similar to CONTRL, and are thus not presented, more significant differences in the vertical structure are apparent in line-averaged cross sections of NOICE. The line-averaged vertical motion at 2 h in NOICE[4] is compared in Fig. 17 to the line-averaged vertical velocity in CONTRL at 3 h. Common features include a secondary maximum in the convective updraft, and the presence of a mesoscale updraft and downdraft. Previous numerical studies that have employed warm-rain microphysical parameterizations (e.g., Dudhia et al. 1987; Fovell and Ogura 1988; Redelsperger and Lafore 1988) have also found that ice processes are not essential for simulation of multicellular convective updrafts. We find, however, that inclusion of the ice phase significantly modifies the structure of the convective region and allows it to more closely resemble the observations in this case (Fig. 14). The modifications include a deeper low-level updraft at the leading edge in CONTRL, less rearward tilt of this updraft, and the significantly higher elevation (10 km MSL) of the secondary updraft maximum to its rear.

5. Influence of physical parameterizations on cold pool structure

Since rearward tilt of convective systems has been linked to cold pool strength (e.g., Weisman 1992; his Fig. 2), we now examine the cold pool structure of the line-averaged cross sections for each of the three simulations. In each case, the line-averaged cold pools exhibit their greatest depth over a 25-km region associated with convective precipitation that begins at the leading edge (Fig. 18). Rearward of this zone, the cold pool depth, as delineated by the -0.5 K θ' contour, decreases to 400 m (roughly one-third of its maximum depth) in the region of lighter stratiform precipitation. The simulations that include MCS-induced fluxes (Figs. 18a,c) exhibit a more rapid surface warming with distance from the leading edge and a more realistic reduced static stability within the lowest levels of the cold pool that results from more intense turbulent mixing induced by the fluxes. The shallow surface-based ~200-m-deep mixed layer observed in the stratiform precipitation region (LeMone et al. 1995) is much closer to being reproduced in these simulations than in experiment NOFLUX (cf. Figs. 18a,c with Fig. 18b). The coldest surface temperature perturbations are found in NOFLUX (Fig. 18b), ranging from a minimum of -4°C near the leading edge of the convective precipitation to -2.5°C at the back edge of the light surface stratiform precipitation near the left end of the cross section. However, comparison of CONTRL (Fig. 18a) with NOFLUX (Fig. 18b) reveals that, near the leading edge of the squall line, the warmer temperatures in CONTRL are limited to a shallow 300-m depth.

---

[4] We constructed a line-averaged cross section for the more rapidly evolving simulation NOICE 1 h earlier than for CONTRL and NOFLUX so that we could compare the vertical structure from the different experiments at similar stages of development.

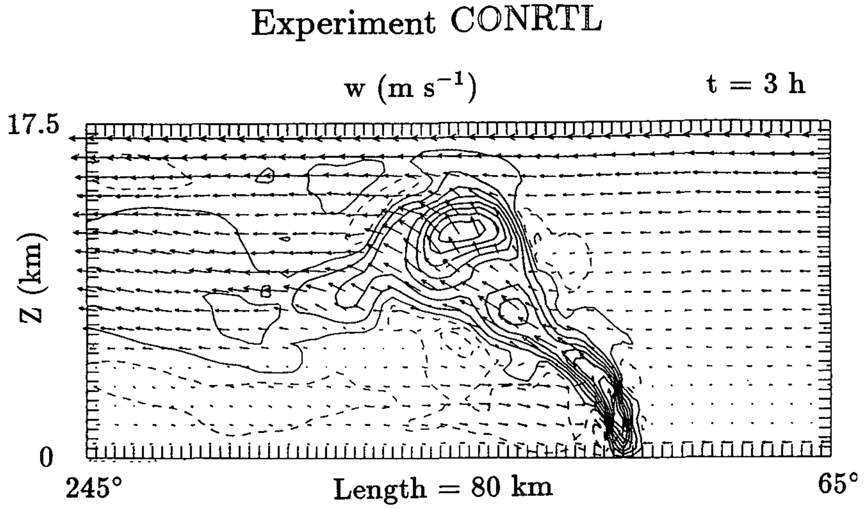

FIG. 15. Vertical velocity (1 m s^{-1} contour intervals; positive values solid, negative values dashed, zero line omitted; thin solid and dashed contours enclose areas exceeding 0.25 m s^{-1} and less than −0.25 m s^{-1}, respectively) and approximate system-relative flow in the plane of a vertical cross section A–A' along azimuth 245°–65° near the center portion of the updraft in experiment CONTRL at 3 h in Fig. 12a. The vertical scale is exaggerated 2:1.

Near the leading edge, where the cold pool interacts with the ambient vertical shear and directly influences convective organization, the deepest cold air is found in NOICE (Fig. 18c).

The Rotunno et al. (1988) criterion for development of upshear tilt[5] in squall lines is satisfied when the square root of twice the vertically integrated negative buoyancy of the cold pool exceeds the difference (vertical shear) in the ambient line-normal wind speed from the surface through a depth equal to that of the cold pool. Since this ambient vertical shear is equivalent in each of the simulations, differences in the cold pool buoyancy near its leading edge can be used to explain differences in updraft tilt. Mean values of the total buoyancy

$$B = g\left[\frac{\theta'}{\bar{\theta}(z)} + 0.61q_v' - q_c - q_r - q_i - q_s - q_g\right],$$

calculated through a cold pool depth of 2 km for the line-averaged cross sections of each simulation, are displayed in Fig. 19. The substantially greater mean negative buoyancy evident in the NOICE cold pool is consistent with the greater rearward tilt of the associated convective system (Fig. 17). The vertically integrated negative buoyancy is proportional to the square of the cold pool propagation speed c within the approximation of Rotunno et al. (1988). Thus, it is not surprising that c is ~2 m s^{-1} greater for NOICE than for both CONTRL and NOFLUX for the period between 2 and 3 h. Further examination of Fig. 19 reveals that the proportion of cold pool negative buoyancy due to water loading varies from 20%–30% at the leading edge to 10%–15% at back edge of the convective region and is nearly equal in magnitude among the three simulations at the times of the cross sections. The greater negative buoyancy at the leading edge of NOICE is, thus, due to a deeper and stronger mean temperature deficit within the cold pool.

The interaction between cold pool negative buoyancy and environmental vertical shear is most applicable for explaining the early development of rearward tilt in MCSs as has been done in our current discussion. We note, however, that the theory of Rotunno et al. (1988) assumes no relative motion within the cold pool and thus excludes the horizontal vorticity associated with the internal cold pool circulation (Lafore and Moncrieff 1989; Weisman 1992). In the mature stages of MCSs, internal mesoscale circulations are well developed and may substantially alter the updraft structure expected from considering the Rotunno et al. criterion alone. For example, circulation associated with intrusion of elevated rear inflow into the cold pool (Fig. 16b), which beneath the rear-inflow jet opposes that associated with the horizontal buoyancy gradients at the leading edge of the cold pool (Weisman 1992), may contribute to a decrease in rearward tilt below the rear inflow jet axis and an increase in rearward tilt

---

[5] In the Rotunno et al. study, the upshear direction is relative to the low-level environmental wind profile. In the current study, we use the terminology "rearward tilt" since it precludes ambiguity that might arise due to variation in the direction of the environmental vertical shear vector with height associated with the jet profile of Fig. 2.

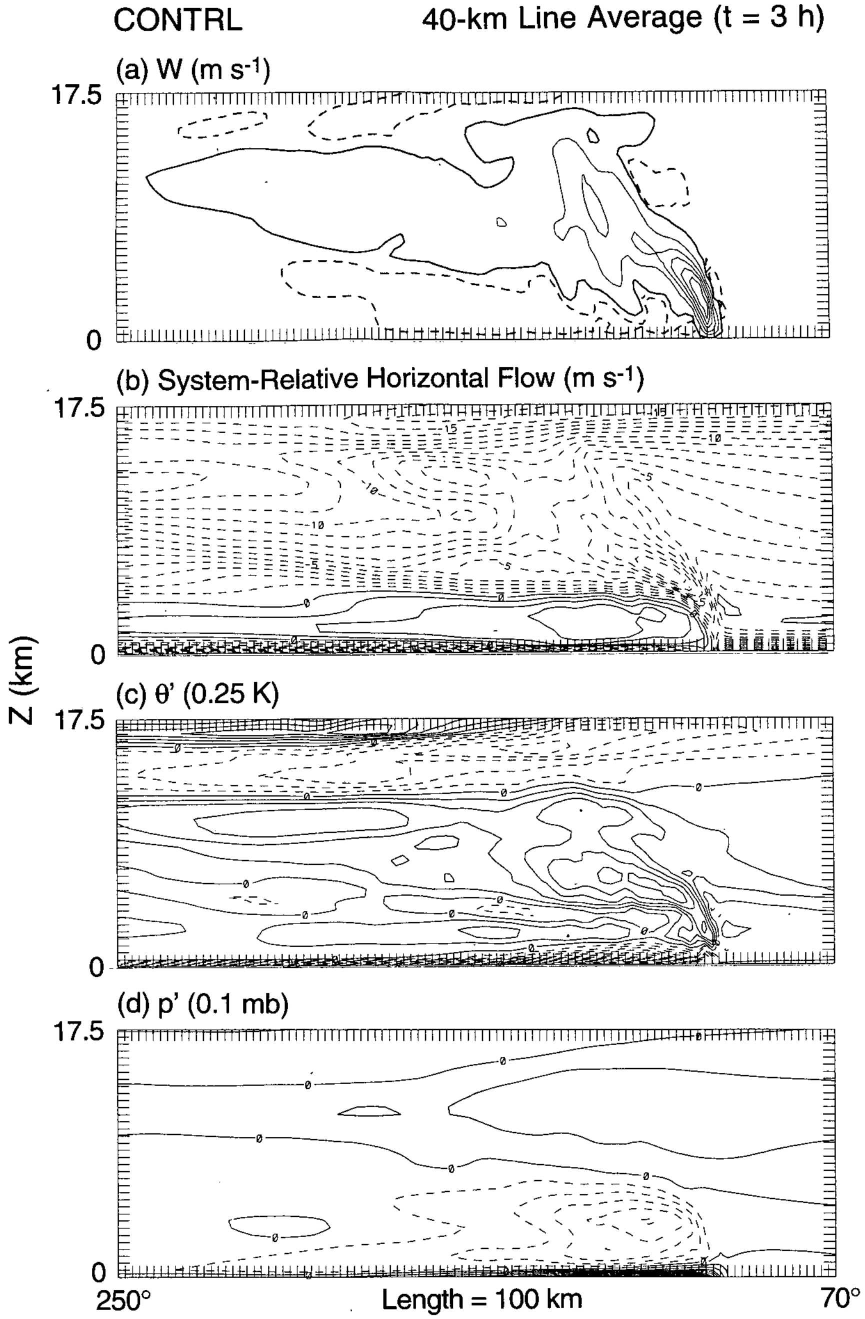

FIG. 16. As in Fig. 13 but for (a) vertical velocity (thin lines are 1 m s^{-1} contour intervals, zero line omitted; bold solid contours enclose values exceeding 0.1 m s^{-1}, bold dashed contours enclose values below −0.1 m s^{-1}); (b) approximate system-relative flow in the plane of the cross section (1 m s^{-1} contour intervals); (c) potential temperature perturbation from initial conditions (0.25 K contour intervals); and (d) pressure perturbation from initial conditions (0.1-mb contour intervals).

above it. The important influences of internal mesoscale circulations on updrafts in CONTRL will be described in more detail in a future paper.

Additional factors not considered in the current analysis may also influence rearward tilt. Fankhauser et al. (1992) noted that while its relative impact is

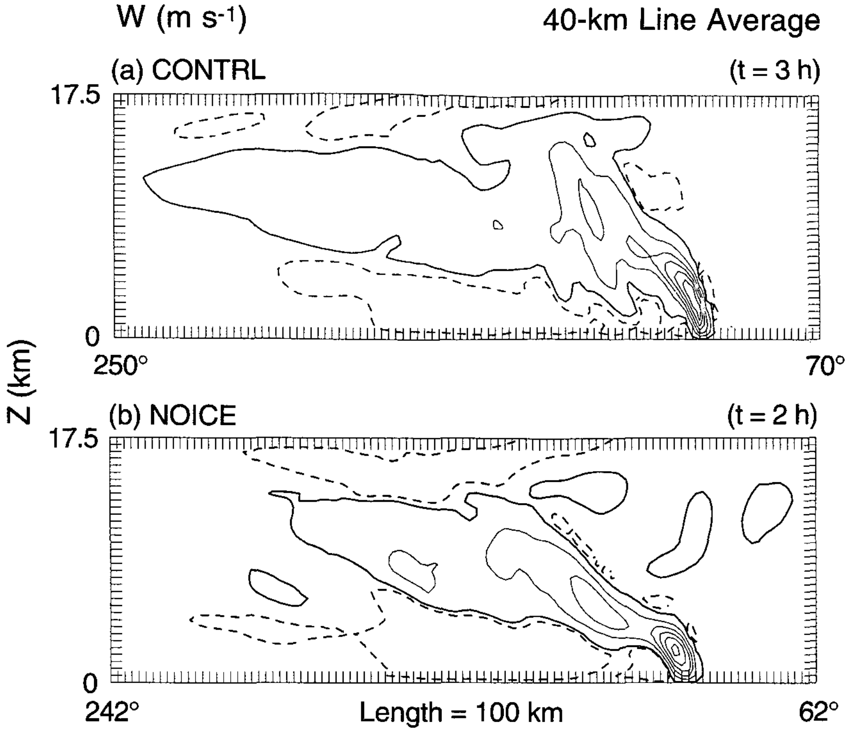

FIG. 17. Vertical cross section of vertical velocity from 40-km averages (a) along azimuth 340°–160° in experiment CONTRL for the center portion of the leading-edge updraft at 3 h enclosed by the brackets in Fig. 12a and (b) along azimuth 332°–152° in experiment NOICE for the center portion of the leading edge updraft at 2 h enclosed by the brackets in Fig. 12c. Contour intervals are as in Fig. 16a. In each panel the vertical scale is exaggerated 2:1.

difficult to quantify, surface stress should oppose circulation generated by horizontal buoyancy gradients at the cold pool edge. The effect of surface stress within the cold pool would be to decrease updraft tilt at low levels. However, surface stress does not appear to be a dominant factor influencing the updraft tilt in the current simulations since it is included in both CONTRL and the much more strongly rearward-tilted NOICE experiment. In each of the current simulations the ambient reverse shear above the jet axis (Fig. 2) augments the rearward tilt as suggested in earlier studies (e.g., Weisman et al. 1988; Szeto and Cho 1994a).

While the mean cold pool strength during the linear stage is significantly greater in NOICE, the cold pool in CONTRL continues to intensify through 5 h and eventually exceeds that of NOICE. Szeto and Cho (1994b) also found stronger cold pools during the early stages of their ice-free two-dimensional simulations of midlatitude squall lines. They attributed the stronger cold pool to large terminal velocities associated with heavy rain, causing an anomalous concentration of precipitation and presumably greater evaporative cooling near the leading edge. McCumber et al. (1991) showed larger domain-averaged convective rainfall for the early stages of their two-dimensional simulations of tropical squall lines with warm-rain microphysics. They explained that the suspension of graupel particles in updrafts due to their smaller terminal velocities delays surface precipitation in simulations that contain ice microphysics. Although the amount of rainfall is not distinctly different between NOICE and the other two simulations at the times of comparisons in Fig. 19, similar mechanisms may be operating. Simplified experiments of single-cell convective storms initiated with the sounding in Fig. 2 indicate that stronger cold pools in warm-rain simulations develop very early, within 40 min of initial updraft formation.

Regardless of the precise mechanism for the stronger cold pool in the early stages of NOICE, a clear distinction between the impact of ice microphysics and MCS-induced fluxes on squall line evolution can be made. Inclusion of ice microphysics begins to significantly influence cold pool strength as soon as deep convection occurs, leading to feedbacks in the structure and evolution of convection. In the case of MCS-induced fluxes, the impact on the cold pool is initially confined to the region near the surface. For instance, the significantly colder surface temperatures in NOFLUX at 3 h (Fig. 18) are not strongly reflected in the mean negative buoyancy of the cold pool (Fig. 19). Only after longer periods of time, or in regions where cold pools are particularly shallow or weak (e.g., the far southern flank in Fig. 9) do the MCS-induced fluxes impact the cold pool to the extent necessary to influence deep convection.

6. Summary and discussion

In this study, we have used a three-dimensional numerical cloud model to simulate a portion of a large tropical squall line that occurred on 22 February 1993 during TOGA COARE. Our idealized experiments were designed to both replicate the observed short-term evolution of the squall line and facilitate study of the sensitivity of the simulated squall line to small-scale physical processes including ice-phase microphysics and MCS-induced surface fluxes and stresses. The implementation of a surface boundary condition that enables vertical fluxes and tangential stresses associated with deep convection to impact the subsequent three-dimensional evolution of the squall line represents a unique aspect of our numerical simulations.

The simulations successfully reproduce many of the observed features of the squall line including the development of a 30-km scale low-to-midlevel vortex and the associated transition from a linear leading edge of deep convection to a pronounced bow-shaped structure. During the earlier linear stage, both the modeled and observed convective region are characterized by rearward tilt and updraft maxima at two heights, the first at low levels adjacent to the leading edge and the second in the upper troposphere ~20 km to the rear. In a future study, we focus on the development of vertical vorticity within the midlevel vortex at the northern end of the simulated bow-shaped convective segment and on the dynamics of convective-scale updrafts within the precipitation system.

Previous studies have illustrated the importance of small-scale physical processes on the long-term mesoscale structure of large precipitation systems. For instance, numerous numerical studies (e.g., Tao and Simpson 1989; Caniaux et al. 1994) have shown that inclusion of the ice phase is crucial for the development of a realistic trailing stratiform region in squall lines. The current study focuses on the shorter-term evolution of tropical squall lines, and more specifically addresses processes influencing convection near the leading edge of these precipitation systems. We find that inclusion of MCS-induced fluxes and stresses and ice microphysics are not needed to replicate gross features of the observed convective region. However, for the relatively weak convectively induced cold pools that occur in our simulations within this tropical oceanic environment, these processes significantly impact both the realism of the aforementioned features and the more general evolution of the squall line in very distinct ways.

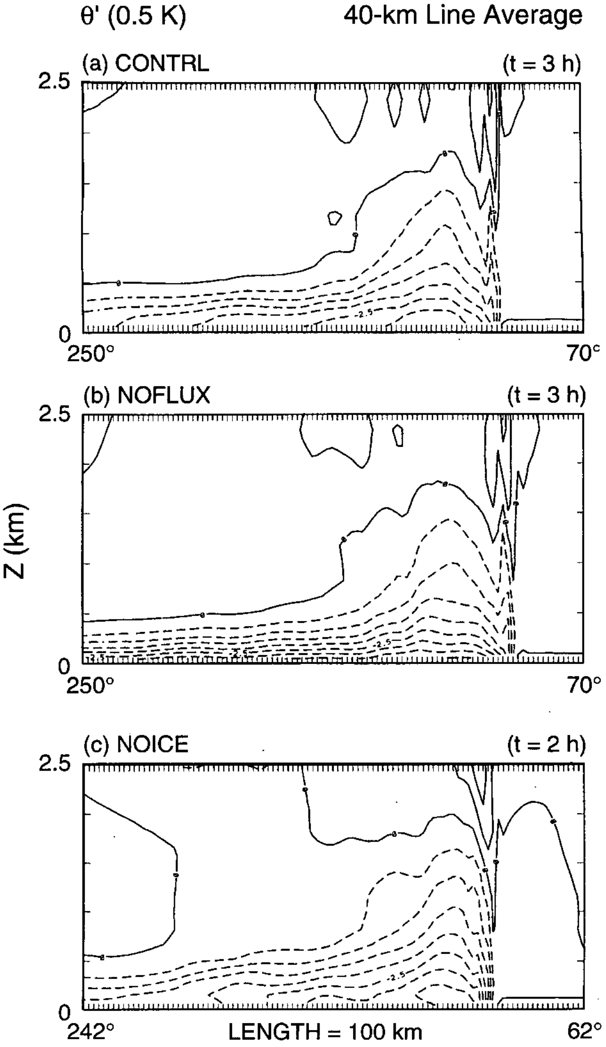

FIG. 18. Vertical cross sections of potential temperature perturbations from initial conditions (0.5 K contour intervals) in the lowest 2.5 km MSL constructed from 40-km averages approximately parallel to the leading edge updraft for (a) the region of experiment CONTRL at 3 h enclosed by the brackets in Fig. 12a, (b) the region of experiment NOFLUX at 3 h enclosed by the brackets in Fig. 12b, and (c) the region of experiment NOICE at 2 h enclosed by the brackets in Fig. 12c. In each panel the vertical scale is exaggerated 20:1.

Inclusion of the ice phase results in both differences in the timing of the transition to a highly three-dimensional morphology and in a more realistic simulation of the precipitation and convective updraft

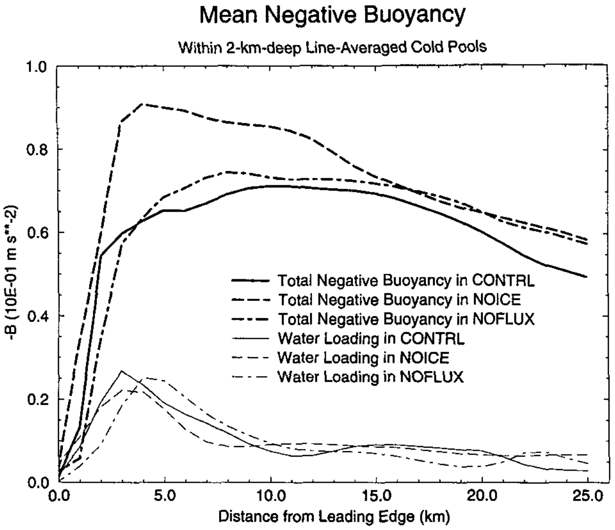

FIG. 19. Total negative buoyancy (bold lines) and the portion of the negative buoyancy due to water loading (thin lines) averaged through a 2-km deep layer constructed from the three cross sections of Fig. 18 for the 25-km horizontal zone at the leading edge of the convectively induced cold pool.

structure. Differences in the tilt of the leading convective updraft region in simulations using different microphysical parameterizations are explained by considering the dynamical interaction between the horizontal vorticity of the ambient vertical shear and horizontal vorticity that arises from horizontal buoyancy gradients at the leading edge of the cold pool (e.g., Rotunno et al. 1988). This interaction is sensitive to differences in the integrated negative buoyancy within the cold pool, which itself is influenced by the different microphysical parameterizations. A deeper low-level updraft and a more realistic reduced rearward tilt of the convective region during its earlier linear stage in simulations that include ice process is consistent with weaker cold pool strengths. Greater storm depths in simplified one-dimensional models of deep convection for this same case in experiments that include ice processes (Lucas et al. 1995) are consistent with the greater depth of the secondary updraft, which is well-removed from the forced lifting near the leading edge, in our three-dimensional simulations that included the ice phase (Fig. 17). Consistent results from these two different approaches suggests that the inclusion of the ice processes may also influence storm depth in a more direct way, through enhanced latent heating that results from freezing in updrafts (e.g., Williams and Renno 1993).

The inclusion of MCS-induced fluxes strongly influences the areal extent of the mesoscale region of boundary-layer cooling and drying in the wake of the squall line. While our flux formulation is highly idealized, mesoscale aspects of the low-level structure in the wake of the leading convective precipitation band are consistent with observations from this case and other studies of large tropical squall lines. The influence of MCS-induced fluxes on deep convection at the leading edge of the squall line is limited to later stages of the simulation. The impact is most pronounced on the far southern flank of the squall line where the cold pool is weak and shallow but ground-relative winds and MCS-induced fluxes are enhanced relative to the northern flank.

The simulations suggest that the MCS-induced surface fluxes and stresses may impact the scale of active convection at the leading edge of squall lines after a significant period of time ($t \sim 4-5$ h). It is important to remember, however, that the current study is idealized in that it assumes a quasi-steady horizontally homogeneous base state. How severely such an assumption is violated over the 6-h timescale (the duration of our simulations) varies from case to case. Also, we stress that these results pertain to large squall lines oriented perpendicular to moderate-to-strong vertical shear associated with a low-level jet. The response of other forms of tropical convection (e.g., slower-moving convective bands oriented primarily parallel to the deep tropospheric vertical shear, or ensembles of more isolated cells) to small-scale processes such as fluxes and ice microphysics, could be different and await investigation.

Acknowledgments. We thank Mary Barth (NCAR) for providing a version of the ice microphysical parameterization code modified for use in these simulations and for providing software used to diagnose reflectivity from model-predicted bulk microphysical quantities. Robert Fovell (UCLA) and two anonymous reviewers are acknowledged for their useful comments and suggestions. Robert Fovell alerted us to the possibility that differences in cold pool strength between the observations and the control simulation could result from differences in the height of downdraft origination within the rear inflows. Conversations with Richard Carbone (NCAR), Richard Johnson (Colorado State University), Sharon Lewis (Cooperative Institute for Research in Environmental Sciences), Joseph Klemp (NCAR), Jean-Luc Redelsperger (Meteo France), Richard Rotunno (NCAR), Bradley Smull (NOAA/National Severe Storms Laboratory), Wei-Kuo Tao (NASA/Laboratory for Atmospheres), Morris Weisman (NCAR), Louis Wicker (Texas A&M University), and Edward Zipser (Texas A&M University) concerning this work are also appreciated. This work was sponsored by the National Science Foundation Grant 9215507.

APPENDIX

Sounding Used to Initialize the Cloud Model

z (m)	P (mb)	θ (K)	q_v (g kg^{-1})	u (m s^{-1})	v (m s^{-1})
50	998.7	299.5	19.8	0.1	−6.5
154	987.0	299.8	19.4	1.2	−6.5
267	974.5	300.2	19.0	2.4	−6.5
389	961.0	300.5	18.6	3.6	−6.5
522	946.6	301.0	18.1	5.0	−6.5
665	931.2	301.4	17.6	6.5	−6.5
821	914.8	302.0	16.8	7.9	−6.4
990	897.2	302.7	15.6	8.9	−6.0
1172	878.4	303.5	14.3	10.1	−5.7
1370	858.5	304.2	13.3	10.9	−5.2
1585	837.3	305.0	12.7	11.5	−4.7
1817	814.8	305.9	12.1	12.0	−4.2
2069	790.9	307.1	11.5	12.1	−3.8
2342	765.8	308.4	10.9	11.9	−3.4
2638	739.3	310.1	10.2	11.3	−3.1
2958	711.5	311.9	9.5	10.7	−2.8
3305	682.4	313.9	8.8	10.0	−2.6
3681	652.0	316.2	8.1	9.4	−2.4
4089	620.4	318.4	7.3	8.8	−2.3
4530	587.6	320.6	6.6	8.0	−2.1
5009	553.7	323.1	5.8	7.2	−1.8
5527	518.8	325.8	5.0	6.4	−1.5
6089	483.1	328.7	4.3	5.6	−1.2
6697	446.8	331.8	3.5	4.9	−0.8
7357	410.0	335.2	2.7	4.1	−0.4
8050	374.1	338.3	1.9	3.3	0.0
8750	340.4	341.2	1.3	2.6	0.6
9450	309.1	343.9	0.9	1.8	1.1
10150	280.2	346.0	0.5	1.1	1.6
10850	253.4	347.5	0.3	0.5	2.0
11550	228.4	348.7	0.1	−0.4	2.3
12250	205.5	350.1	0.0	−1.1	2.6
12950	184.3	351.4	0.0	−1.7	3.1
13650	164.8	352.4	0.0	−2.5	3.5
14350	146.8	353.0	0.0	−3.6	4.2
15050	130.4	355.6	0.0	−4.6	3.9
15750	115.4	358.6	0.0	−5.5	3.5
16450	101.9	364.2	0.0	−6.0	0.8
17150	89.8	377.0	0.0	−5.1	−2.5
17850	79.1	385.5	0.0	−4.9	−2.4
18550	69.5	398.6	0.0	−4.9	−2.4
19250	61.1	411.8	0.0	−4.9	−2.4
19950	53.7	425.0	0.0	−4.9	−2.4
20650	47.2	438.1	0.0	−4.9	−2.4
21350	41.1	451.3	0.0	−4.9	−2.4
22050	36.2	464.4	0.0	−4.9	−2.4
22750	31.7	477.6	0.0	−4.9	−2.4
23450	27.7	490.8	0.0	−4.9	−2.4
24150	24.2	503.9	0.0	−4.9	−2.4

REFERENCES

Arakawa, A., and M.-D. Cheng, 1993: The Arakawa–Schubert cumulus parameterization. *The Representation of Cumulus Convection in Numerical Models, Meteor. Monogr.,* No. 46, Amer. Meteor. Soc., 123–136.

Barnes, G. M., and M. Garstang, 1982: Subcloud layer energetics of precipitating convection. *Mon. Wea. Rev.,* **110,** 102–117.

——, and K. Sieckman, 1984: The environment of fast- and slow-moving tropical mesoscale convective cloud lines. *Mon. Wea. Rev.,* **112,** 1782–1794.

Brandes, E. A., 1990: Evolution and structure of the 6–7 June mesoscale convective system and associated vortex. *Mon. Wea. Rev.,* **118,** 109–127.

Brown, J. M., 1979: Mesoscale unsaturated downdrafts driven by rainfall evaporation: A numerical study. *J. Atmos. Sci.,* **36,** 313–338.

Caniaux, G., J.-L. Redelsperger, and J.-P. Lafore, 1994: A numerical study of the stratiform region of a fast-moving squall line. Part I: General description and water and heat budgets. *J. Atmos. Sci.,* **51,** 2046–2074.

Carbone, R. E., J. W. Conway, N. A. Crook, and M. W. Moncrieff, 1990: The generation and propagation of a nocturnal squall line. Part I: Observations and implications for mesoscale predictability. *Mon. Wea. Rev.,* **118,** 26–49.

Chong, M., P. Amayenc, G. Scialom, and J. Testud, 1987: A tropical squall line observed during the COPT 81 Experiment in West Africa. Part I: Kinematic structure inferred from dual-Doppler radar data. *Mon. Wea. Rev.,* **115,** 670–694.

Clark, T. L., 1979: Numerical simulations with a three-dimensional cloud model: Lateral boundary condition experiments and multicellular severe storm simulations. *J. Atmos. Sci.,* **36,** 2191–2215.

Davis, C. A., and M. L. Weisman, 1994: Balanced dynamics of mesoscale vortices produced in simulated convective systems. *J. Atmos. Sci.,* **51,** 2005–2030.

Dudhia, J., and M. W. Moncrieff, and D. K. W. So, 1987: The two-dimensional dynamics of West African squall lines. *Quart. J. Roy. Meteor. Soc.,* **113,** 121–146.

Durran, D. R., and J. B. Klemp, 1983: A compressible model for the simulation of moist mountain waves. *Mon. Wea. Rev.,* **111,** 2341–2361.

Fairall, C. W., E. F. Bradley, D. P. Rogers, J. B. Edson, and G. S. Young, 1996: Bulk parameterization of air–sea fluxes for TOGA COARE. *J. Geophys. Res.,* **101,** 3747–3765.

Fankhauser, J. C., G. M. Barnes, and M. A. LeMone, 1992: Structure of a midlatitude squall line in strong unidirectional shear. *Mon. Wea. Rev.,* **120,** 237–260.

Ferrier, B. S., W.-K. Tao, and J. Simpson, 1995: A double moment multiple-phase four-class bulk ice scheme. Part II: Simulations of convective storms in different large-scale environments and comparisons with other bulk parameterizations. *J. Atmos. Sci.,* **52,** 1001–1033.

Fovell, R. G., and Y. Ogura, 1988: Numerical simulation of a midlatitude squall line in two dimensions. *J. Atmos. Sci.,* **45,** 3846–3879.

Hoult, D. P., 1972: Oil spreading on the sea. *Annu. Rev. Fluid Mech.,* **4,** 341–368.

Houze, R. A., Jr., 1977: Structure and dynamics of a tropical squall line observed during GATE. *Mon. Wea. Rev.,* **105,** 1540–1567.

——, S. A. Rutledge, M. I. Biggerstaff, and B. F. Smull, 1989: Interpretation of Doppler weather radar displays of midlatitude mesoscale convective systems. *Bull. Amer. Meteor. Soc.,* **70,** 608–619.

Johnson, R. H., and M. E. Nicholls, 1983: A composite analysis of the boundary layer accompanying a tropical squall line. *Mon. Wea. Rev.,* **111,** 308–319.

——, and P. J. Hamilton, 1988: The relationship of surface pressure features to the precipitation and air flow structure of an intense midlatitude squall line. *Mon. Wea. Rev.,* **116,** 1444–1472.

Jorgensen, D. P., and B. F. Smull, 1993: Mesovortex circulations seen by airborne Doppler radar within a bow-echo mesoscale convective system. *Bull. Amer. Meteor. Soc.,* **74,** 2146–2157.

——, T. J. Matejka, D. Johnson, and M. A. LeMone, 1994: A TOGA/COARE squall line seen by multiple airborne Doppler radars. Preprints, *Sixth Conf. on Mesoscale Processes,* Portland, OR, Amer. Meteor. Soc., 25–28.

——, ——, and M. A. LeMone, 1995: Structure and momentum fluxes within a TOGA/COARE squall line system observed by airborne Doppler radar. Preprints, *21st Conf. on Hurricanes and Tropical Meteorology,* Miami, FL, Amer. Meteor. Soc., 579–581.

Keenan, T. D., and R. E. Carbone, 1992: A preliminary morphology of precipitation systems in northern Australia. *Quart. J. Roy. Meteor. Soc.,* **118,** 283–326.

Kessler, E., 1969: *On the Distribution and Continuity of Water Substance in Atmospheric Circulations. Meteor. Monogr.,* No. 32, Amer. Meteor. Soc., 84 pp.

Klemp, J. B., and R. B. Wilhelmson, 1978: The simulation of three-dimensional convective storm dynamics. *J. Atmos. Sci.,* **35,** 1070–1096.

——, R. Rotunno, and W. C. Skamarock, 1994: On the dynamics of gravity currents in a channel. *J. Fluid Mech.,* **269,** 169–198.

Lafore, J.-P., and M. W. Moncrieff, 1989: A numerical investigation of the convective region and stratiform regions of tropical squall lines. *J. Atmos. Sci.,* **46,** 521–544.

Leary, C. A., and R. A. Houze Jr., 1979a: The structure and evolution of convection in a tropical cloud cluster. *J. Atmos. Sci.,* **36,** 437–457.

——, and ——, 1979b: Melting and evaporation of hydrometeors in precipitation from the anvil clouds of deep tropical convection. *J. Atmos. Sci.,* **36,** 669–679.

LeMone, M. A., 1980: The marine boundary layer. *Workshop on the Planetary Boundary Layer,* J. C. Wyngaard, Ed., Amer. Meteor. Soc., 182–234.

——, G. M. Barnes, and E. J. Zipser, 1984a: Momentum fluxes by lines of cumulonimbus over the tropical oceans. *J. Atmos. Sci.,* **41,** 1914–1932.

——, ——, E. J. Szoke, and E. J. Zipser, 1984b: The tilt of the leading edge of mesoscale tropical convective lines. *Mon. Wea. Rev.,* **112,** 510–519.

——, D. P. Jorgensen, S. Lewis, B. Smull, and T. Matejka, 1995: Boundary layer recovery in the stratiform region of mesoscale convective systems in TOGA COARE. Preprints, *21st Conf. on Hurricanes and Tropical Meteorology,* Miami, FL, Amer. Meteor. Soc., 509–511.

Lin, X., and R. H. Johnson, 1996: Kinematic and thermodynamic characteristics of the flow over the Western Pacific warm pool during TOGA COARE. *J. Atmos. Sci.,* **53,** 695–715.

Liu, W. T., K. B. Katsaros, and J. A. Businger, 1979: Bulk parameterization of air–sea exchanges of heat and water vapor including the molecular constraints at the interface. *J. Atmos. Sci.,* **36,** 1722–1735.

Loehrer, S. M., and R. H. Johnson, 1995: Surface pressure and precipitation life cycle characteristics of PRE-STORM mesoscale convective systems. *Mon. Wea. Rev.,* **123,** 600–621.

Lucas, C., E. J. Zipser, and B. S. Ferrier, 1995: Warm-pool cumulonimbus and the ice phase. Preprints, *Conf. on Cloud Physics,* Dallas, TX, Amer. Meteor. Soc., 318–320.

McCumber, M., W.-K. Tao, J. Simpson, R. Penc, and S.-T. Soong, 1991: Comparison of ice-phase microphysical parameterization schemes using numerical simulations of tropical convection. *J. Appl. Meteor.,* **30,** 985–1004.

Miller, M. J., A. C. M. Beljaars, and T. N. Palmer, 1992: The sensitivity of the ECMWF model to the parameterization of evaporation from the tropical oceans. *J. Climate,* **5,** 418–434.

Newton, C. W., 1950: Structure and mechanism of the prefrontal squall line. *J. Meteor.,* **7,** 210–222.

Parsons, D., and Coauthors, 1994: The integrated sounding system: Description and preliminary observations from TOGA COARE. *Bull. Amer. Meteor. Soc.,* **75,** 553–567.

Redelsperger, J.-L., and J.-P. Lafore, 1988: A three-dimensional simulation of a tropical squall line: Convective organization and thermodynamic vertical transport. *J. Atmos. Sci.*, **45**, 1334–1356.

Rickenbach, T., 1995: Rainfall production from the spectrum of convection observed by shipboard radar during TOGA COARE. Preprints, *21st Conf. on Hurricanes and Tropical Meteorology*, Miami, FL, Amer. Meteor. Soc., 116–118.

Rotunno, R., and K. A. Emanuel, 1987: An air–sea interaction theory for tropical cyclones. Part II: Evolutionary study using a nonhydrostatic axisymmetric numerical model. *J. Atmos. Sci.*, **44**, 542–561.

——, J. B. Klemp, and M. L. Weisman, 1988: A theory for strong, long-lived squall lines. *J. Atmos. Sci.*, **45**, 463–485.

Rutledge, S. A., and P. V. Hobbs, 1984: The mesoscale and microscale structure and organization of clouds and precipitation in midlatitude cyclones. Part XII: A diagnostic modeling study of precipitation in narrow cold-frontal rainbands. *J. Atmos. Sci.*, **41**, 2949–2972.

——, R. A. Houze Jr., M. I. Biggerstaff, and T. Matejka, 1988: The Oklahoma–Kansas mesoscale convective system of 10–11 June 1985: Precipitation structure and single-Doppler radar analysis. *Mon. Wea. Rev.*, **116**, 1409–1430.

Scott, J. D., and S. A. Rutledge, 1995: Doppler radar observations of an asymmetric MCS and associated vortex couplet. *Mon. Wea. Rev.*, **123**, 3437–3457.

Skamarock, W. C., 1989: Truncation error estimates for refinement criteria in nested and adaptive models. *Mon. Wea. Rev.*, **117**, 882–886.

——, and J. B. Klemp, 1993: Adaptive grid refinement for two-dimensional and three-dimensional nonhydrostatic atmospheric flow. *Mon. Wea. Rev.*, **121**, 788–804.

——, M. L. Weisman, and J. B. Klemp, 1994: Three-dimensional evolution of simulated long-lived squall lines. *J. Atmos. Sci.*, **51**, 2563–2584.

Smith, P. L., Jr., C. G. Myers, and H. D. Orville, 1975: Radar reflectivity factor calculations in numerical cloud models using bulk parameterization of precipitation processes. *J. Appl. Meteor.*, **14**, 1156–1165.

Smull, B. F., and R. A. Houze Jr., 1985: A midlatitude squall line with a trailing region of stratiform rain: Radar and satellite observations. *Mon. Wea. Rev.*, **113**, 117–133.

——, and ——, 1987: Dual-Doppler radar analysis of a midlatitude squall line with a trailing region of stratiform rain. *J. Atmos. Sci.*, **44**, 2128–2148.

Szeto, K. K., and H.-R. Cho, 1994a: A numerical investigation of squall lines. Part II: The mechanics of evolution. *J. Atmos. Sci.*, **51**, 425–433.

——, and ——, 1994b: A numerical investigation of squall lines. Part III: Sensitivity to precipitation processes and the Coriolis force. *J. Atmos. Sci.*, **51**, 1341–1351.

Tao, W.-K., and J. Simpson, 1989: Modeling study of a tropical squall-type convective line. *J. Atmos. Sci.*, **46**, 177–202.

——, ——, and S.-T. Soong, 1991: Numerical simulation of a subtropical squall line over the Taiwan Strait. *Mon. Wea. Rev.*, **119**, 2699–2723.

Thorpe, A. J., M. J. Miller, and M. W. Moncrieff, 1982: Two-dimensional convection in nonconstant shear: A model of midlatitude squall lines. *Quart. J. Roy. Meteor. Soc.*, **108**, 739–762.

Wang, T.-C. C., Y.-J. Lin, R. W. Pasken, and H. Shen, 1990: Characteristics of a subtropical squall line determined from TAMEX dual-Doppler data. Part I: Kinematic structure. *J. Atmos. Sci.*, **47**, 2357–2381.

Webster, P. J., and R. Lukas, 1992: TOGA COARE: The Coupled Ocean–Atmosphere Response Experiment. *Bull. Amer. Meteor. Soc.*, **73**, 1377–1416.

Weisman, M. L., 1992: The role of convectively generated rear-inflow jets in the evolution of long-lived mesoconvective systems. *J. Atmos. Sci.*, **49**, 1827–1847.

——, 1993: The genesis of severe long-lived bow-echoes. *J. Atmos. Sci.*, **50**, 645–670.

——, and J. B. Klemp, 1986: Characteristics of isolated convective storms. *Mesoscale Meteorology and Forecasting*, P. Ray, Ed., Amer. Meteor. Soc., 390–413.

——, ——, and R. Rotunno, 1988: Structure and evolution of numerically simulated squall lines. *J. Atmos. Sci.*, **45**, 1990–2013.

Wicker, L. J., and R. B. Wilhelmson, 1995: Simulation and analysis of tornado development and decay within a three-dimensional supercell thunderstorm. *J. Atmos. Sci.*, **52**, 2675–2703.

Williams, E., and N. Renno, 1993: An analysis of the conditional instability of the tropical atmosphere. *Mon. Wea. Rev.*, **121**, 21–36.

Young, G. S., S. M. Perugini, and C. W. Fairall, 1995: Convective wakes in the equatorial western Pacific during TOGA. *Mon. Wea. Rev.*, **123**, 110–123.

Zipser, E. J., 1977: Mesoscale and convective-scale downdrafts as distinct components of squall line structure. *Mon. Wea. Rev.*, **105**, 1568–1589.